CSIRO PUBLISHING

RESEARCH PAPER
https://doi.org/10.1071/WF22013

International Journal of WILDLAND FIRE
International Association of Wildland Fire

Coupled fire-atmosphere simulation of the 2018 Camp Fire using WRF-Fire

Kasra Shamsaei[A], Timothy W. Juliano[B], Matthew Roberts[C], Hamed Ebrahimian[A,*], Branko Kosovic[B], Neil P. Lareau[C] and Ertugrul Taciroglu[D]

For full list of author affiliations and declarations see end of paper

*Correspondence to:
Hamed Ebrahimian
Department of Civil and Environmental Engineering, University of Nevada-Reno, 1664 N. Virginia Street, Reno, NV 89557, USA
Email: hebrahimian@unr.edu

Received: 17 February 2022
Accepted: 30 November 2022
Published: 5 January 2023

Cite this:
Shamsaei K *et al.* (2023)
International Journal of Wildland Fire
doi:10.1071/WF22013

ABSTRACT

Background. Accurate simulation of wildfires can benefit pre-ignition mitigation and preparedness, and post-ignition emergency response management. **Aims.** We evaluated the performance of Weather Research and Forecast-Fire (WRF-Fire), a coupled fire-atmosphere wildland fire simulation platform, in simulating a large historic fire (2018 Camp Fire). **Methods.** A baseline model based on a setup typically used for WRF-Fire operational applications is utilised to simulate Camp Fire. Simulation results are compared to high-temporal-resolution fire perimeters derived from NEXRAD observations. The sensitivity of the model to a series of modelling parameters and assumptions governing the simulated wind field are then investigated. Results of WRF-Fire for Camp Fire are compared to FARSITE. **Key results.** Baseline case shows non-negligible discrepancies between the simulated fire and the observations on rate of spread (ROS) and spread direction. Sensitivity analysis results show that refining the atmospheric grid of Camp Fire's complex terrain improves fire prediction capabilities. **Conclusions.** Sensitivity studies show the importance of refined atmosphere modelling for wildland fire simulation using WRF-Fire in complex terrains. Compared to FARSITE, WRF-Fire agrees better with the observations in terms of fire propagation rate and direction. **Implications.** The findings suggest the need for further investigation of other possible sources of wildfire modelling uncertainties and errors.

Keywords: Camp Fire, coupled fire-atmosphere simulation, FARSITE, NEXRAD, sensitivity, wildfire simulation, wind, WRF-Fire.

Introduction

In recent years, both the size and the intensity of wildfires have grown, partially due to the effects of climate change (Westerling *et al.* 2006; Littell *et al.* 2009; Abatzoglou and Williams 2016; Westerling 2016). On average, 2.8 million ha of land in the US have been burned by 72 400 wildfires each year since 2000, which is more than double the average hectares burned by wildfires between 1980 and 1999 (https://www.nifc.gov/fire-information/statistics). Aside from the burned lands, wildfires also have economic burdens such as the cost of suppression, loss of properties, and the cost of health impacts related to air pollution caused by wildfires. In 2018, for instance, the California wildfires resulted in an estimated US$148.5 billion of economic damage (Wang *et al.* 2021). Accurate simulations of wildland fire propagation can inform decision making related to pre-ignition preparedness and mitigation and post-ignition emergency response management. Furthermore, accurate wildfire simulations, together with simulations of the wind field, can provide a forecast of wildfire smoke dispersion (Li *et al.* 2020; Rooney *et al.* 2020). Such a capability can eventually play a critical role in limiting the health impacts of wildland fires. However, due to the complex multi-physics nature of the wildfire combustion process, fire interactions with land surface features and atmosphere, and various modelling uncertainties and errors, accurate simulation of the fire propagation process remains a challenge.

Current wildland fire modelling approaches can be categorised into three groups: (1) semi-empirical models without fire-atmosphere coupling; (2) semi-empirical models with fire-atmosphere coupling; and (3) physics-based models. The first category uses semi-empirical models, such as Rothermel's rate of spread (ROS) (Rothermel 1972) model, to propagate the surface fire (e.g. FARSITE (Finney 1998) and ELMFire (Lautenberger 2013)). These models can run on relatively coarse grids, require low computational demands, and are currently widely used for operational wildland fire simulation in the U.S. Nevertheless, they suffer from the lack of coupling between the fire and atmosphere and thus, cannot predict fire-induced winds, which may alter the rate and direction of fire spread. The second category includes the semi-empirical fire spread model with the fire-atmosphere coupling (e.g. WRF-Fire (Coen *et al.* 2013)). In this approach, an atmospheric model based on computational fluid dynamics is used to simulate the atmospheric state and the fire-atmosphere coupling, resulting in more realistic simulations compared to the first category. Moreover, while these models require higher spatial resolution than the first category, they have been used for operational purposes as a result of algorithmic scalability and recent advances in High-Performance Computing (Giannaros *et al.* 2020). Finally, the third modelling category includes physics-based models, which directly solve the combustion process (e.g. FIRETEC (Linn 1997) and WFDS (Mell *et al.* 2007)). More suited for research applications, these models resolve the physical processes governing the combustion, require a high-resolution domain, and are computationally demanding. WRF-Fire, which stands in the second category, is chosen for this study as the wildfire simulation platform due to the reasonable compromise between computational demand and adequate representation of the fire propagation process.

WRF-Fire is a wildland surface fire spread forecast model within Advanced Research WRF (ARW) atmospheric model (Mandel *et al.* 2011; Coen *et al.* 2013). Further details on WRF-ARW and WRF-Fire are presented in the WRF atmospheric and WRF-Fire wildfire simulation platforms section. In recent years, a number of studies have been conducted to validate WRF-Fire, assess its sensitivity to various modelling parameters, and guide prescribed burns. WRF-SFIRE, which is a version of WRF-Fire, was used to simulate the FireFlux prescribed-burn experiment, and the simulation results were compared to various field measurements (Kochanski *et al.* 2012). The study concluded that the ability of WRF-SFIRE in predicting fire arrival time to the measurement towers and fire-atmosphere coupling is reasonable. However, due to the measured data limitations, the model performance could not be evaluated comprehensively. In another study, WRF-SFIRE fire forecast results (e.g. the fire spread direction and burned area predictions) were used to decide about sensor placement in the FireFlux II prescribed burn experiment (Clements *et al.* 2019).

The sensitivity of WRF-Fire configured in Large Eddy Simulation (LES) to several modelling parameters, including fuel type and wind speed, is investigated in a study by Coen *et al.* (2013). The study, however, was limited to small idealised flat domains. The effects and importance of LES in simulating Low Intensity Prescribed Fire (LIPF) experiments, which took place in New Jersey, were investigated in Lai *et al.* (2020). This study showed that WRF-Fire could produce more realistic and accurate results when configured in the LES mode. Two Santa Ana fires from 2007 were simulated using WRF-SFIRE (Kochanski *et al.* 2013), which showed the ability of WRF-SFIRE to forecast the fire propagation with reasonable accuracy and computational demand, making it suitable for operational purposes. Moreover, the study showed that the simulation accuracy highly depends on the simulated wind field, and WRF atmospheric model may overestimate weak winds and cannot capture the hourly variations of wind direction. Another study investigated the potential of using WRF-Fire in simulating a high-impact fire, Chimney Tops II Fire (Jiménez *et al.* 2018*a*). The study demonstrated that high-resolution coupled fire-atmosphere simulation of Chimney Tops II fire could provide forecasts of potential fire propagation process and pointed to the challenges presented by long-range spot fire ignitions. Currently, no study exists in the literature that comprehensively evaluates the sensitivity of WRF-Fire to modelling parameters and its performance in simulating large-scale historic fires in high-resolution LES configuration.

The main objective of this study is to examine the performance and the accuracy of the WRF-Fire platform in simulating large-scale wildland fires, as well as the sensitivity of the simulation platform to several modelling parameters and assumptions. Here, WRF-Fire is used to simulate and study the 2018 Camp Fire, the deadliest and most destructive wildfire in California history. Aside from the societal impact of this historic fire, the availability of radar-estimated high-temporal-resolution fire perimeters (Lareau *et al.* 2022) provides an outstanding opportunity to compare WRF-Fire simulation results with real-world fire behaviour and to overcome the shortcoming of previous studies in which the comparison of simulation results with low-spatial and low-temporal resolution fire perimeter observations cannot portray the complete history of simulation-observation discrepancies as also mentioned in Kochanski *et al.* (2013).

These radar-based perimeters are estimated from local maxima in radar reflectivity, which is associated with Pyrometeors loading in updrafts rising from regions of active combustion. The radar estimates for the Camp Fire (and other fires) compare well with sporadically available infrared observations from satellite (e.g. VIIRS) and airborne (e.g. NIROPs) sensors but provide higher temporal and spatial resolution (e.g. 10 min, 250 m) and thus, enable more specific error identification in the simulated fire spread. While uncertainty in the radar estimates can arise

due to displacement of the smoke column from the fire at the surface, in the case of the Camp Fire, the radar scans are 'ground skimming,' thus minimising these uncertainties and making the data suitable for model validation.

Furthermore, the sensitivity of the model to a series of modelling parameters and assumptions governing the simulated wind field is investigated. The sensitivity analyses provide insights into the performance and challenges of wildland fire prediction with coupled fire-atmosphere models such as WRF-Fire and can guide the simulation of wind-driven fires in complex terrains.

The structure of the rest of this paper is as follows. In the first two sections, the 2018 Camp Fire and the WRF-Fire simulation platform are briefly introduced. Next, the model parameterisation for Camp Fire sensitivity studies is explained in the Model setup section. The results of the sensitivity analysis are presented in the Results. The WRF-simulated wind field is compared to several Remote Automatic Weather Stations (RAWS) following the Results section. Next, WRF-Fire simulations are compared to FARSITE for Camp Fire. The computational demand of Camp Fire case studies for both WRF-Fire and FARSITE is presented in the Computational demand section. Lastly, the findings are summarised in the Discussion section, followed by a Summary and Conclusions.

Camp Fire

The Camp Fire started on the morning of 8 November 2018 around 06:20 hours Pacific Standard Time (PST) near the community of Pulga in Butte County, CA due to failure of electrical transmission lines. The Camp Fire lasted for about 18 days before being completely contained, with most of the damage occurring in the first 24 h of fire growth. It burned a total of 62 053 ha, destroyed 18 804 structures, and resulted in 85 civilian fatalities and several firefighter injuries. The low fuel moisture content and dangerous fire conditions, including strong downslope winds, low humidity, and warm temperatures (Brewer and Clements 2020; Mass and Ovens 2021), resulted in an explosive fire rapidly burning to the east into Pulga and to the west into Concow, Paradise, Magalia, and the outskirts of east Chico (Maranghides *et al.* 2021). With the overall estimated loss of US$16.6 billion, the Camp Fire is the most destructive and deadliest fire so far in California history and the costliest natural disaster worldwide in 2018 (Maranghides *et al.* 2021).

The Camp Fire was first reported by a civilian call to 911 around 06:25 hours (PST). The fire quickly became well established in steep canyon terrain moving toward Concow at around 07:00 hours (PST), and the main fire front reached Pentz road at around 08:30 hours (PST). Camp Fire generated about 30 spot fires in Paradise before 08:30 hours (PST). Most of the spot fires were within 1 km of wildland, while some spots reached as far as 3.4 km into Paradise. The spot fires in Paradise were well-established in the town between 09:00 hours and 10:00 hours (PST), and the civilians were stuck on Pentz, Bille, and Pearson roads due to the impacts of the fire. The detailed fire progression timeline is described in NIST's Camp Fire report (Maranghides *et al.* 2021), and the final fire perimeter, along with the topography of its area, is shown in Fig. 1.

In this study, the WRF-Fire version 4.2.2 wildland fire simulation platform is used, and WRF-Fire is slightly modified to support Scott and Burgan's 40 fuel model (Scott and Burgan 2005). The Camp Fire is simulated from 06:00 hours to 17:00 hours (PST), 8 November 2018, which is the fire's main progression time span. The results of WRF-Fire are compared to the fire boundaries identified from NEXRAD radar observations as it provides estimates of fire perimeter in high temporal resolution (i.e. every 15 min).

WRF atmospheric and WRF-Fire wildfire simulation platforms

The Advanced Research WRF (ARW) dynamical core is a widely used community mesoscale Numerical Weather Prediction (NWP) system designed for both atmospheric research and operational forecasting applications (Skamarock *et al.* 2008). The model serves a wide range of meteorological applications across scales from tens of metres to thousands of kilometres. Numerical domains in WRF-ARW are usually divided into several nested domains, with an increasing mesh resolution from the outer to inner domains. Recent developments expanded the application of WRF-ARW to multi-scale simulations, bridging mesoscale, where turbulent fluxes are parameterised, and microscales, where large turbulent eddies are resolved (e.g. Muñoz-Esparza *et al.* 2014, 2017; Mazzaro *et al.* 2017; Haupt *et al.* 2019).

The multiscale simulation approach is used to simulate Camp Fire. The outer coarse meteorological domain allows

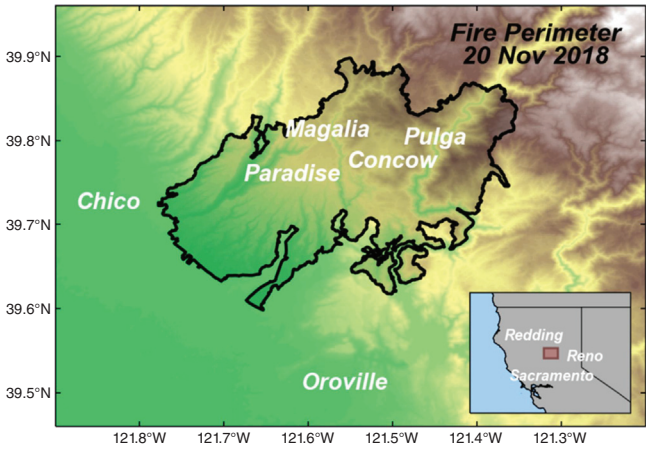

Fig. 1. Final perimeter of Camp Fire (black line) along with topography (coloured contour).

the WRF model to capture large synoptic flows that feed the fine inner domains, which are run in LES to capture and simulate small flows and turbulent eddies. Furthermore, features such as land use and topography are static data used in the WRF model to simulate the wind field, which is one of the key components affecting fire propagation. WRF-ARW also uses a terrain-following vertical grid to better represent the airflow over topography. The nested domains and detailed land surface setup, together with the other features and capabilities of WRF-ARW, such as radiation and microphysics schemes, provide the ability of localised weather prediction at significantly finer resolutions than currently available weather data such as those obtained from the HRRR (Benjamin *et al.* 2016) forecast system and ERA5 (Hersbach *et al.* 2020) reanalysis.

Input data and steps to create and run WRF and WRF-Fire simulations are shown in Fig. 2. In general, the input data, which consists of land coverage and topography map, fuel map (for WRF-Fire only), and forcing data are passed through the WRF Preprocessing System (WPS), and the resulting preprocessed data are fed to the WRF platform, which consists of WRF-ARW and WRF-Fire. The results can then be post-processed using various methods such as VAPOR (Visualization & Analysis Systems Technologies 2022) or in-house scripts with the aid of WRF-Python (Ladwig 2017), which is used in this study. Further information on the input data and model creation can be found in WRF's User's Guide (WRF 2020) and WRF-Fire Wikipage (Shamsaei *et al.* 2022).

WRF-Fire is a two-way coupled atmosphere-wildland surface fire simulation platform. The fire spread model in WRF-Fire is based on Rothermel's semi-empirical Rate of Spread (ROS) model (Rothermel 1972) within the Advanced Research WRF (ARW) dynamical core (Mandel *et al.* 2011; Coen *et al.* 2013). The fire behaviour model does not simulate the physical processes governing the combustion, but instead uses the semi-empirical Rothermel ROS model to advance fire perimeter. As a two-way coupled wildland fire-atmosphere model, the fire behaviour model receives the wind components from the WRF atmospheric model to propagate the fire and feeds the sensible and latent heat flux back to the atmospheric model to disturb the atmosphere state allowing the fire to 'create its own weather' (Mandel *et al.* 2011; Coen *et al.* 2013), a feature that is not available in other commonly used operational wildland fire simulation platforms such as FARSITE (Finney 1998), which is an uncoupled surface fire propagation platform based on the Rothermel's ROS model and Huygen's wave principle (Miller 1991). The computational process at each time step is summarised in the next paragraph.

At each time step, the local wind components at the fire line along with the surface fuel characteristics and topography gradients are used to calculate the local fire ROS using Rothermel's model, then the fire is propagated on the surface using a level-set implementation of the local ROS (Muñoz-Esparza *et al.* 2018). After advancing the fire, the amount of fuel consumed by the fire is calculated using a semi-empirical algorithm that characterises the fuel consumption rate for different fuel types (Mandel *et al.* 2011). Next, the sensible and latent heat fluxes are calculated using the consumed fuel and fuel moisture content. The calculated sensible and latent heat fluxes are then inserted, respectively, as temperature and water vapour tendencies into the vertical levels of the WRF atmospheric model using an exponential decay height. These tendencies will impact the atmospheric flow, modifying both the wind speed and direction.

Model setup

Sensitivity studies in this paper are focused on three main modelling assumptions (Table 1): (1) forcing weather model; (2) spin-up time; and (3) domain resolution. For the effects of the forcing weather model, the baseline model is initialised using High-Resolution Rapid Refresh (HRRR) (Benjamin *et al.* 2016) forecasting system, and the fire propagation results are compared to another case study

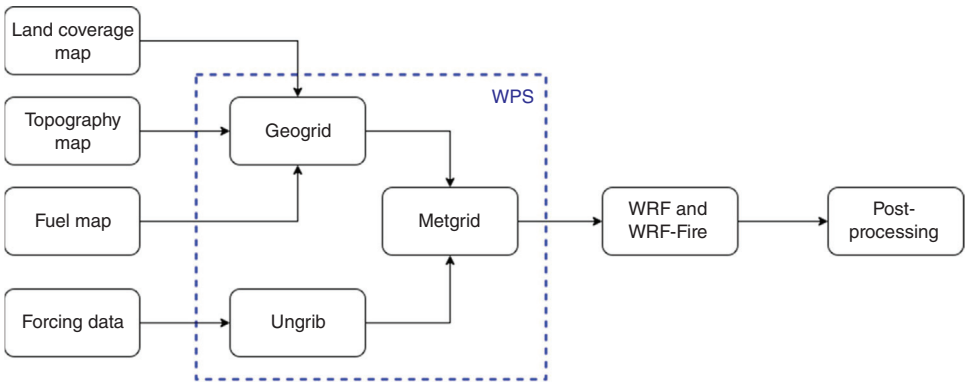

Fig. 2. Steps to produce WRF-Fire simulations in real data cases.

Table 1. Case studies for Camp Fire sensitivity analysis.

Case study	Abbreviation	Domain setup	Weather model	Spin-up time
Baseline	Base	2-domain	HRRR	25 min
Effects of weather	Weath1	2-domain	ERA5	25 min
Effects of spin-up time	Spin3	2-domain	ERA5	3 h
	Spin6	2-domain	ERA5	6 h
Effects of domain resolution	3dom	3-domain	ERA5	25 min
	3domspin3	3-domain	ERA5	3 h

that uses the fifth generation of ECMWF Reanalysis (ERA5) (Hersbach *et al.* 2020) product. For the effects of spin-up time, three case studies with 25 min (baseline), 3 and 6 h of spin-up are considered. For the effects of domain resolution, the 111 m atmospheric grid in the baseline case (Fig. 3*a*) is further refined using a 3-domain setup (Fig. 3*b*) in order to increase the innermost domain resolution to match the 30 m topographic map. The effects of spin-up time are also investigated in the 3-domain setup using 25 min and 3 h of spin-up. Further details on the model setup and modelling assumptions are provided in the following paragraphs.

The baseline model setup chosen for this study is based on the assumptions often used in operational wildfire simulations by Colorado Fire Prediction System (CO-FPS) (Jiménez *et al.* 2018*a*, 2018*b*; Knievel *et al.* 2020). It has two one-way nested domains with 1 km and 111 m grid sizes (i.e. the parent to child grid ratio is nine) (Fig. 3*a*). While larger than usual values of three or five, the ratio is set to nine and kept constant throughout this study to avoid simulation in the so-called 'Terra Incognita' (Wyngaard 2004), where neither one-dimensional Planetary Boundary Layer (PBL) parameterisations nor LES are appropriate (Muñoz-Esparza *et al.* 2017). Furthermore, WRF's nesting capability is used to resolve turbulent eddies and develop a well-mixed boundary layer. The parent and the child domains are 270 by 360 km and 30 by 40 km, respectively (i.e. 360 and 270 grid cells in X and Y directions, respectively, in both domains). Both domains are centred at (39.75°N, 121.55°W), hence covering parts of northern California and Nevada (Fig. 3*a*). The outermost domain uses MYNN Level 2.5 (Nakanishi and Niino 2006) PBL parameterisation to represent turbulent mixing in the boundary layer while the fine inner domain is configured in LES mode (i.e. PBL parameterisation is turned off and 3D 1.5-order TKE closure sub-grid scale mixing scheme is activated) to allow resolving the turbulent eddies (Bauer *et al.* 2020).

To achieve a well-mixed boundary layer in LES mode, the WRF atmospheric model must run for what is referred to as the spin-up time prior to the fire simulation. The baseline case simulation is initiated 25 min prior to the fire ignition at 06:25 hours (PST). Moreover, vertical levels include 46 exponentially spaced levels based on operational applications of WRF-Fire as increasing the number of vertical levels increases the computational demand. The lowest vertical level is located at about 7 m above ground level (AGL). The fire mesh is located in the innermost domain, which is four times finer than the child domain to allow for better resolution of fire perimeter and consequent heat and moisture release. To represent the terrain, a 100 m resolution topography map is used in the outer domain. In the inner domain, due to the complex terrain of the area, 30 m resolution topography from the NASA SRTM database is used for representing the topography more accurately and allowing the atmospheric model to better simulate the wind field over the complex terrain. The time-step size in the parent domain is 2 s and the parent-to-child time step ratio is nine.

Other modelling parameters and assumptions are as follows. The land coverage is set using 2011 National Land Coverage Database (NLCD 2011) (Homer *et al.* 2015), and the surface is parameterised using Noah land-surface model (Chen and Dudhia 2001), and the Revised Monin–Obukhov surface layer scheme (Jiménez *et al.* 2012). The Dudhia shortwave radiation (Dudhia 1989), Rapid Radiative Transfer Model (RRTMG) longwave radiation (Iacono *et al.* 2008), Xu-Randall cloud fraction (Xu and Randall 1996), and WRF Single-Moment 6-class (WSM6) microphysics (Hong *et al.* 2004) are activated in all domains. In the outer domain the vertical turbulent mixing is calculated by the PBL, and the horizontal diffusion is calculated using horizontal Smagorinsky first-order closure (Deardorff 1972). However, in the inner domain, full 3D 1.5-order Turbulent Kinetic Energy (TKE) (Deardorff 1980) closure is used to calculate the eddy coefficients. The positive-definite advection scheme for moisture, scalars, and TKE is used in all the domains. Moreover, sixth-order positive-definite horizontal hyper diffusion scheme (Knievel *et al.* 2007), which acts as a numerical noise filter, is also activated in all the domains.

The 2014 LANDFIRE fuel data that classifies surface fuel using Scott and Burgan 40-category fuel classifications (Scott and Burgan 2005) is used in all simulations (Fig. 4). The 2014 fuel map is the closest fuel data to the simulation date. Although LANDFIRE also offers 2020 fuel data, it includes fire disturbances, meaning that the disturbances caused by the 2018 Camp Fire are included in the 2020 fuel data. Therefore, the 2020 fuel data is deemed to be unsuitable for this study. All the fuel categories are assumed to be static fuels, and the fuel moisture content is assumed to be temporally and spatially constant at 8%, which is the typical value in fuel classifications literature. Based on the NIST's Camp Fire report (Maranghides *et al.* 2021), the fire is ignited from a point source located at (39.815°N, 121.434°W), where the faulty transmission line is believed to ignite the fire.

(*a*)

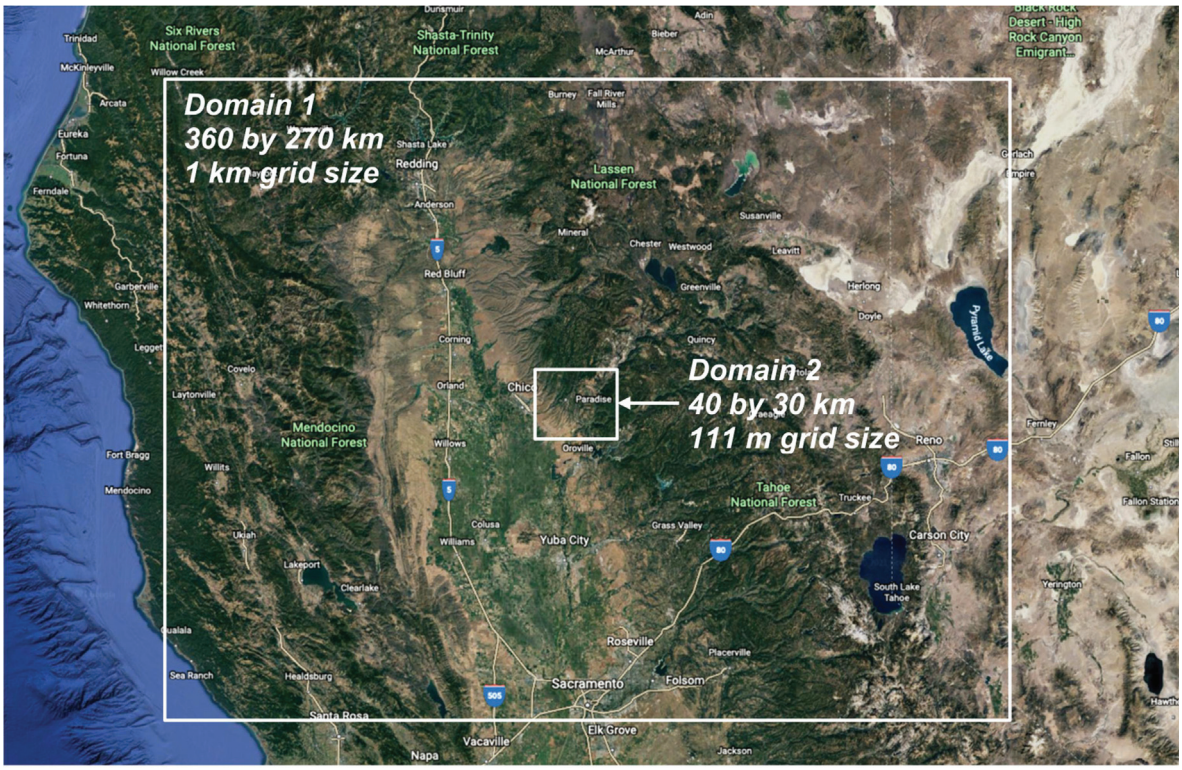

(*b*)

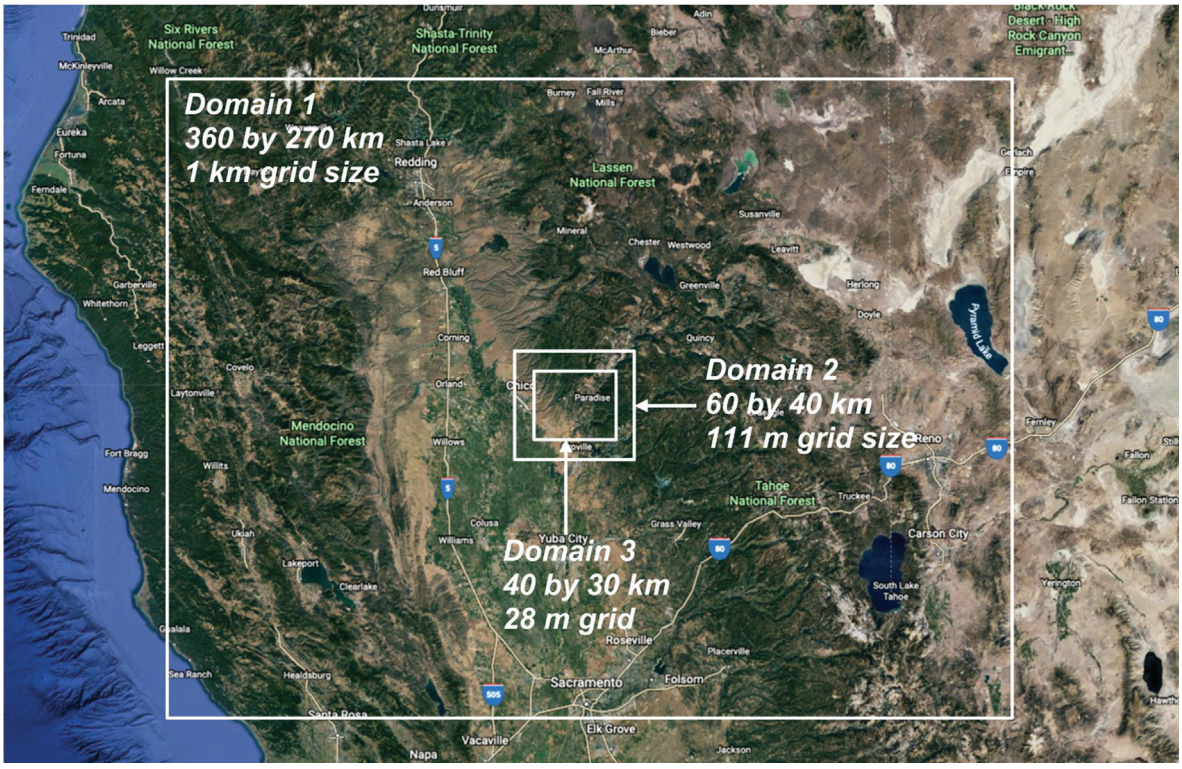

Fig. 3. (*a*) 2-domain and (*b*) 3-domain setup for Camp Fire simulations.

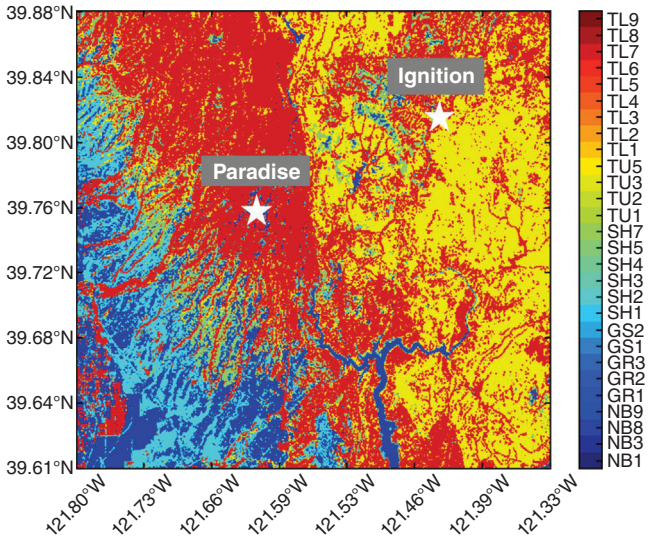

Fig. 4. Fuel map for Camp Fire simulations from 2014 LANDFIRE data. Fuel acronyms are based on Scott and Burgan's 40 fuel categories (Scott and Burgan 2005).

The level-set equation governing the fire propagation process is spatially and temporally discretised using a fifth-order weighted essentially non-oscillatory (WENO5) scheme and third-order explicit Runge–Kutta temporal integration (Muñoz-Esparza *et al.* 2018), respectively. The level-set reinitialisation scheme of WRF-Fire is turned on in all the simulations, and the reinitialisation equation is solved for one iteration at each time step (Muñoz-Esparza *et al.* 2018). The height at which the wind components are calculated for Rothermel's model, which is called the fire wind height, is set to 6.5 m. To calculate the wind components at the fire wind height, an extrapolation option is used to avoid creating artificial feedback loops between the fire and wind. The artificial feedback loop is caused by modification of wind speed at half-flame length used in the rate of spread model as a result of heat release and resulting flow field convergence or divergence from the fire. This can result in an increase in horizontal wind speed that then results in an increased ROS and a larger heat release that can result in a further increase in the rate of spread (i.e. a positive feedback loop), leading to an unrealistic ROS value. In this study, the wind at the fire wind height is calculated using the extrapolation scheme from the wind components at a reference height (60 m), where the effects of flow field convergence or divergence and modifications of horizontal wind speed are less affected by the fire compared to the half-flame length level.

The WRF atmospheric model is initialised using the initial wind speed, wind direction, temperature, and water vapour content of the air provided by the forcing weather model. The lateral boundary condition of the outermost domain is also imposed at 60 min intervals using the forcing model throughout the simulation. The baseline case uses HRRR forcing data, while all other sensitivity analyses utilise ERA5 forcing data. HRRR is an hourly updated, cloud-resolving, convection-allowing operational weather prediction system that covers Contiguous U.S. HRRR horizontal resolution is 3 km with 50 vertical levels, and it is initialised by 3 km grids with 3 km radar assimilation every 15 min (Benjamin *et al.* 2016). ERA5 (Hersbach *et al.* 2020) is a reanalysis product available in hourly intervals. Its accuracy is improved by post-processing observations not available to a forecasting system in real time. ERA5 horizontal grid resolution is 30 km with 137 vertical levels from the surface to 80 km AGL. ERA5 data is available to the users with about 5 days of delays, whereas HRRR data is available in real time.

The 3-domain setup (Fig. 3*b*) is similar to the baseline 2-domain setup, except the inner domain resolution is refined to match the resolution of the topography map, and a second nest (i.e. middle domain) is added to smooth the downscaling from the outer domain to the inner domain. For the 3-domain, the parent-to-child ratio of the middle and the inner domains are nine and four, resulting in the grid size of 111 and 28 m for the middle and the inner domains, respectively. The middle domain size is 60 km × 40 km (i.e. 540 and 405 grid cells in X and Y directions, respectively), and the inner domain size is 40 km × 30 km (i.e. 1080 and 810 grid cells in X and Y directions, respectively). The terrain is presented in the middle domain using the same 100 m topography map as the outer domain. The time step of the outermost domain is 2 s, and the parent-to-child time step ratio is nine and four, resulting in a time step of about 0.22 and 0.05 s in the middle and inner domains.

Results

Baseline case

The initial atmospheric state of the outer domain, including geopotential height, temperature, relative humidity, and wind field derived from the HRRR forcing model, is presented in Fig. 5 at 850 and 500 mb (1 mb = 100 Pa) pressure levels. At 850 mb level, very strong, near-surface pressure-driven flow is present in the domain (i.e. the wind is directed across the geopotential height contours so that the flow is from high pressure to low pressure). The flow can be considered highly ageostrophic and has a substantial downslope component over the fire area (i.e. the wind is blowing from higher to lower terrain). Accompanying this flow regime, a strong west-to-east gradient in relative humidity is apparent, reflecting the adiabatic warming and drying of the air mass as it descends the western slopes of the Sierra Nevada. Combined, the strong near-surface winds and low humidity set the stage for explosive fire growth. At 500 mb level, strong geostrophic northwesterly flow is apparent. The performance of the HRRR

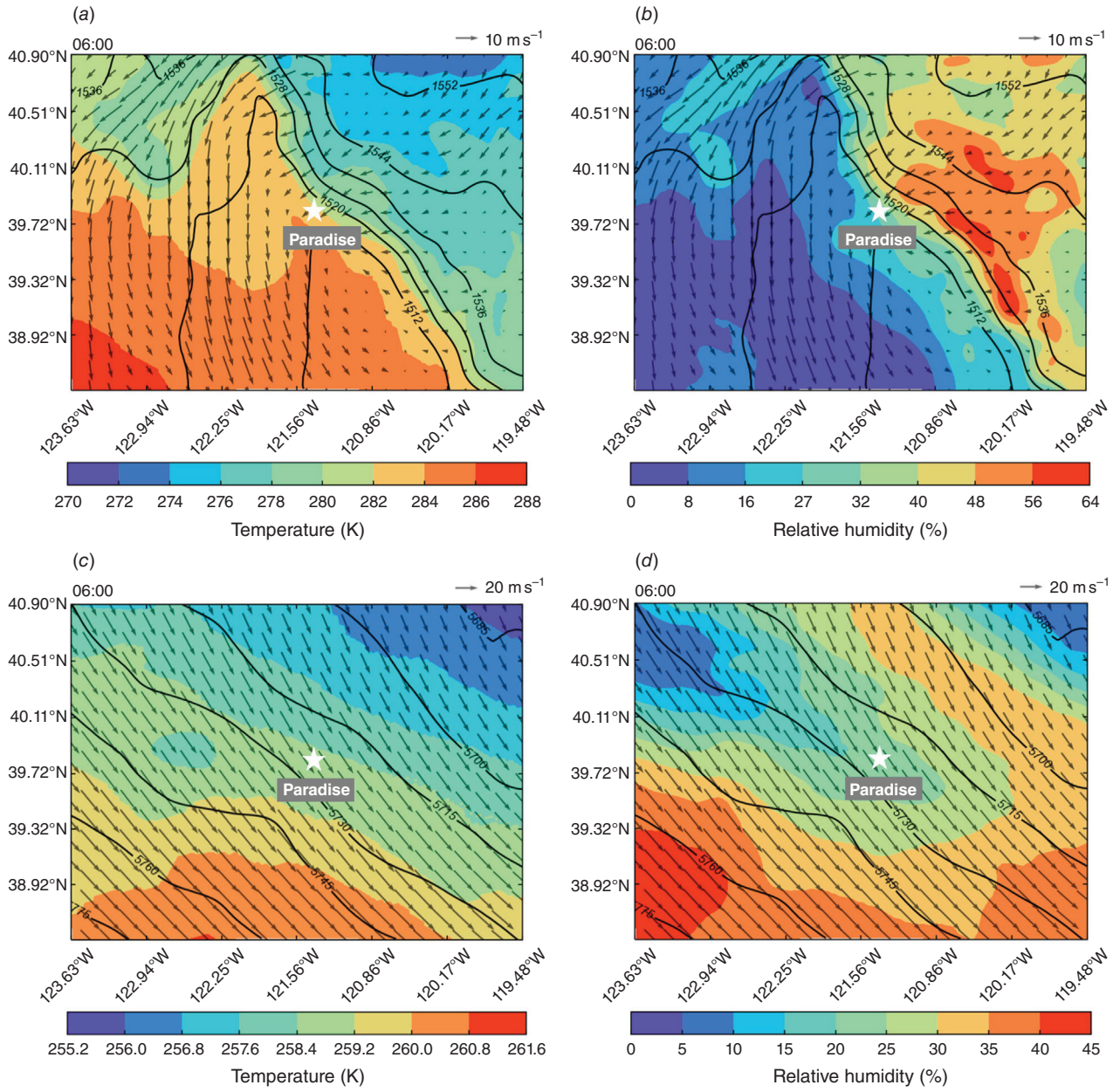

Fig. 5. Initial atmospheric state in the outermost domain of the baseline case derived from the HRRR forcing model. (*a*) Temperature and (*b*) relative humidity at 850 mb, and (*c*) temperature and (*d*) relative humidity at 500 mb pressure levels (1 mb = 100 Pa). Contours and arrows represent geopotential height (m) and wind field, respectively.

model during the Camp Fire event is discussed in Mass and Ovens (2021), which concludes the HRRR's ability to provide an accurate simulation of wind field.

The fire propagation in the baseline model is compared to radar-driven observed Camp Fire boundaries in Fig. 6, setting the stage for the follow-up sensitivity analyses. The simulated fire propagates slower and more to the south-southwest than the observed fire. While the simulated fire boundary better matches the observed boundary near the end of the simulation, the rate and direction of spread differ from observations at the beginning of the simulation. Moreover, the simulated fire passes Route 70 (to the south), likely due to inaccurate fuel map pixels – since WRF-Fire lacks the ability to simulate spotting, the fire spread should theoretically stop at the no fuel boundaries. This can also be seen in Fig. 4 where Route 70 is not identified as non-burnable fuel category. Furthermore, several island-like fire perimeters are evident in this figure, which is due to the presence of non-burnable fuel pixels (e.g. small lakes) that cannot be burned.

To further investigate the fire spread, an along-wind cross-section (red line in Fig. 6) showing the head-fire

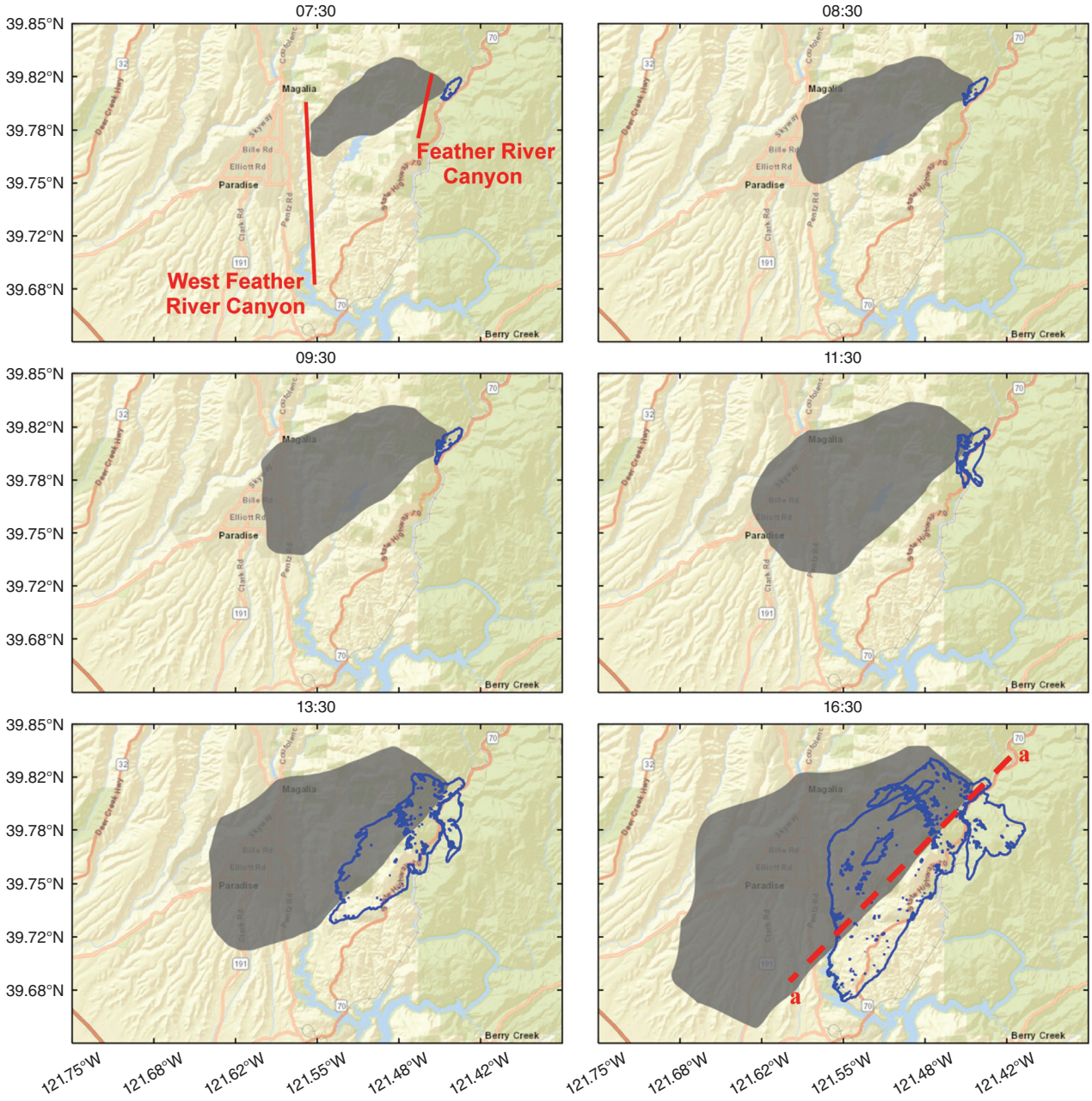

Fig. 6. Comparison of the snapshots of simulated fire perimeter for the baseline case (blue line) with radar-driven observed fire perimeter (grey shading). The related PST time is indicated for each subplot. Red solid lines show Feather River and West Feather River canyons. Red dashed line shows the a–a cross-section used to show fire location on the terrain and ROS.

location with respect to the topography and a time-history of ROS at the fire head are shown in Fig. 7. The head-fire ROS is calculated using the Euclidean distance of head-fire locations at two consecutive output intervals divided by the 15 min output interval. These data show that the simulated fire has a slow ROS at the Feather River and West Feather River canyons located at (39.81°N 121.44°W) and (39.75°N 121.56°W), respectively (also shown in Fig. 6). In fact, the simulated ROS decreases to below 0.1 $m\,s^{-1}$ in the first canyon around 08:00 hours (PST), causing the fire progression to stall until 10:30 hours (PST). The fire then creeps uphill (i.e. ROS of ~0.2 $m\,s^{-1}$) until it passes the summit and accelerates with maximum ROS of ~3 $m\,s^{-1}$ until it reaches the West Feather River canyon at ~15:30 hours (PST), where it again stalls in the valley bottom until the end of the simulation (17:00 hours; PST). This contrasts with the observed fire, which never slowed and propagated through Paradise.

The reason for the slow spread at the two canyons is likely due to the simulated wind conditions at the fire

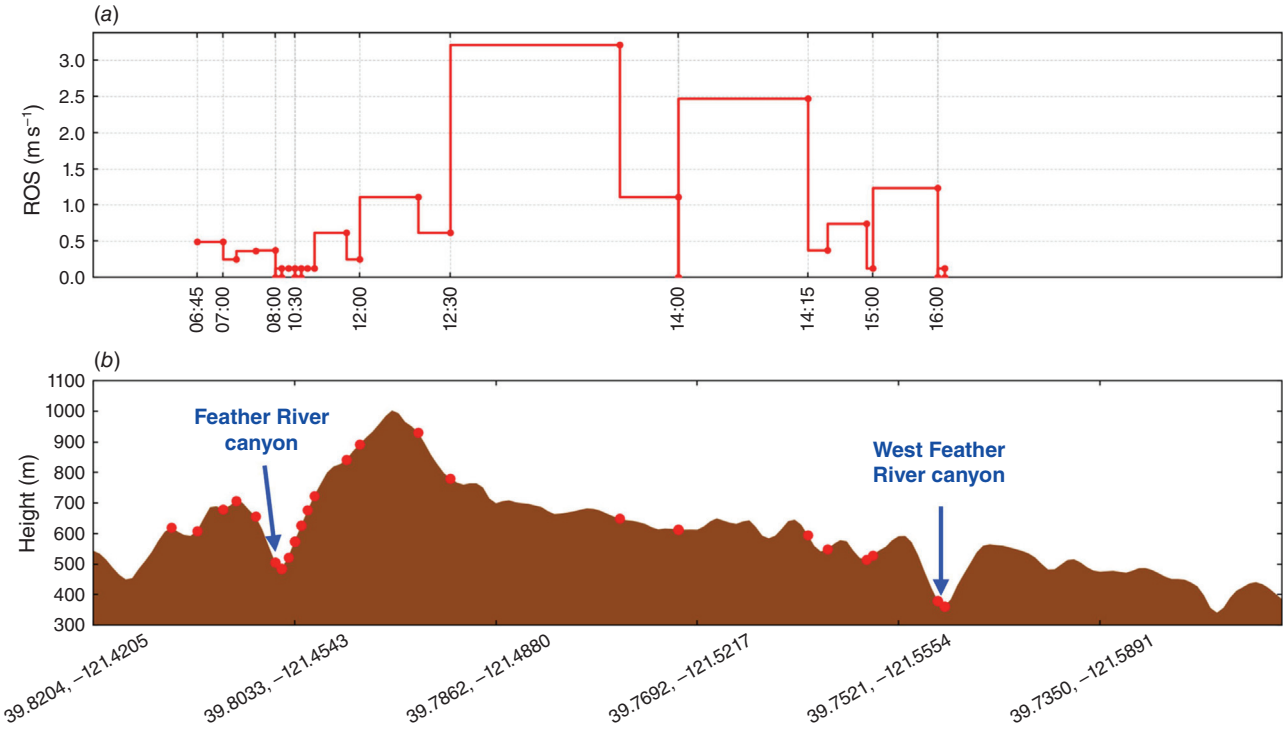

Fig. 7. Time history of the simulated fire head (*a*) ROS and (*b*) location along a–a cross-section in the baseline case (see Fig. 6). Red circles in both figures indicate the fire head, and brown shading shows the terrain.

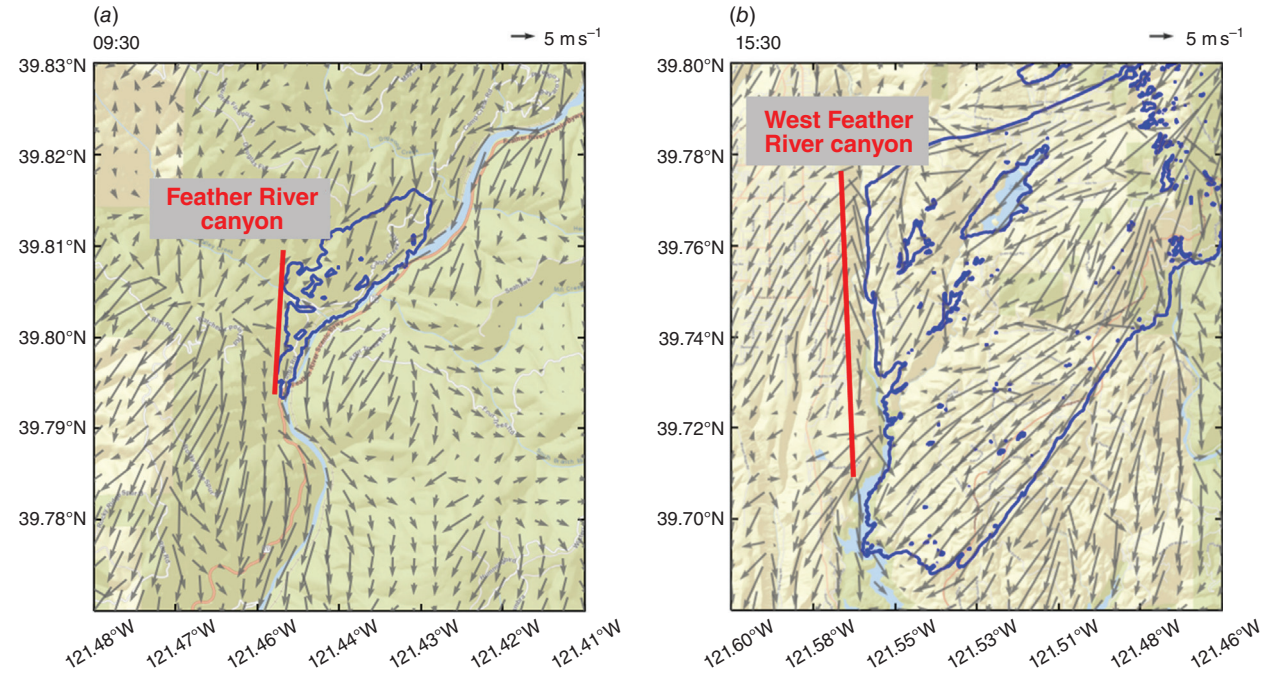

Fig. 8. The simulated wind field at (*a*) Feather River and (*b*) West Feather River canyons in the Camp Fire baseline case.

head. To investigate this, we examine the near-surface wind fields when the fire stalls in the canyons (Fig. 8). Notably, the wind vectors in the two canyons are either parallel to or against the fire line, causing the fire to propagate either parallel to the canyon axis or stall instead of ascending the unburned side of the canyon. This issue indicates that the WRF-ARW atmospheric model either fails to simulate the wind field accurately at the two canyons or a different

process drives the fire across or out of the canyons (e.g. spotting).

Since the vector wind modulates fire spread rate and direction, we infer that wind errors can be one of the likely sources of spread errors. Possible errors in the simulated wind field can be due to: (1) improper representation of the terrain considering the complex terrain of the canyons area; (2) lack of spin-up time, which prevents the atmospheric model from resolving the terrain; (3) improper initial and lateral conditions; and (4) errors from computing wind field in steep terrain due to the WRF-ARW's terrain-following coordinate. To further investigate the effects of the wind field on fire propagation, a series of modelling parameters and assumptions controlling the simulated wind field are chosen for the sensitivity analysis. In the next sub-sections, the effects of: (1) forcing model; (2) spin-up time; and (3) atmospheric grid resolution are investigated.

Effects of forcing model

The forcing model can affect the simulated wind field since it provides the initial atmospheric state and lateral boundary conditions for WRF. To study these effects, the baseline case, initialised from HRRR, is repeated here using ERA5 reanalysis, dubbed 'Weath1' henceforth (see Table 1).

Fig. 9 presents the difference between the initial atmospheric state of the outer domain in Weath1, derived from the ERA5 forcing model, and the baseline, derived from the HRRR forcing model. At 850 mb level, the figure shows that the temperature of both cases is almost similar with the difference that the Weath1 case is slightly warmer (i.e. <2 K on average) and slightly cooler (i.e. <3 K on average) on the north-east and west side of the domain, respectively. In contrast, the relative humidity on the east side of the domain differs in the two cases, and the Weath1 case shows, on average, about 20% less humid structure. In terms of the wind field, the wind speed and direction of the two cases are different, and in some parts of the domain, the wind speed is about 5 m s^{-1} larger in the ERA5 forcing model as compared to the HRRR forcing model. At 500 mb level, however, the atmospheric state and the flow of both cases are almost identical. The temperature variation is below 1 K, and the maximum wind speed difference is about 1–2 m s^{-1}. The relative humidity is almost the same as the baseline case, except the Weath1 case is about 20% less humid than the baseline case on a small part of the west side of the domain. The different atmospheric states at lower vertical levels (e.g. 850 mb level) can affect the simulated atmospheric state and thus, the fire spread process.

Fig. 10 shows the time history of head fire ROS and its respective location for the Weath1 case study. Though the fire still slows down in the Feather River canyon and stops at West Feather River canyon, the fire stalls in the first canyon for a shorter period (08:00–09:45 hours; PST) compared to the baseline case (08:00–10:45 hours; PST). The fire in the Weath1 case also passes the hill after the Feather River canyon faster than the baseline case and reaches the summit around 11:00 hours (PST). Similar to the baseline case, the fire in the Weath1 model propagates rapidly downhill after passing the summit with a maximum ROS of about 2.5 m s^{-1}. The Weath1 case reaches the West Feather River canyon at around 14:30 hours (PST) compared to the baseline case arrival time of 16:00 hours (PST), and finally, the fire stops at the second canyon as it did in the baseline case.

Fig. 11 shows the comparison of the snapshots of the simulated fire perimeter of the Weath1 model with radar-driven observed fire perimeter. It should be noted that the fire perimeter of all the cases is almost identical from 07:30 hours to 09:30 hours (PST) resulting in overlapping fire perimeters. When comparing the overall fire perimeter in baseline and Weath1 cases in Fig. 11, there is a non-negligible difference between the two forcing models. For both models, fire propagates slower than the radar-observed boundaries at the beginning of the simulation until 09:30 hours (PST). The primary direction of the fire propagation is similar in the two cases, although the Weath1 case also generates north and north-westerly flanks in contrast to the baseline case. This lateral uphill movement better matches the observed fire progression, though the overall fire direction and ROS still differ substantially from the radar-observed fire perimeter. Despite these differences, Weath1 compares more favourably to the observations and therefore, the rest of the sensitivity studies use ERA5 forcing and initialisation. In the next step, the effects of spin-up time, which can help the WRF atmospheric model to better resolve large turbulent eddies and terrain, are investigated.

Effects of spin-up time

The spin-up time allows the innermost LES domain to develop and resolve large turbulent eddies and develop a well-mixed boundary layer. Due to the coarse horizontal resolution of the forcing model (i.e. 30 km in ERA5), the small-scale flow features and turbulent eddies are not resolved in the weather data that feeds the atmospheric model. Accurate prediction of the wildland fire spread in a complex terrain requires resolving terrain-induced circulations and turbulence. However, in multiscale simulations, the turbulence does not develop instantaneously on the inner LES domain since the flow is smooth on the mesoscale domain, resolved with 1 km grid cells. Therefore, to investigate the effects of different spin-up times, three case studies are considered herein: (1) 25 min (baseline case); (2) 3 h (Spin3 model); and (3) 6 h (Spin6 model) of spin-up time.

The fire-height vector winds (at 6.5 m) prior to ignition are shown for the three cases in Fig. 12. The dominant north-easterly wind direction is similar across cases, but the Spin3 and Spin6 cases yield 2–3 times stronger north-easterly flow to the south-west of Paradise as compared to

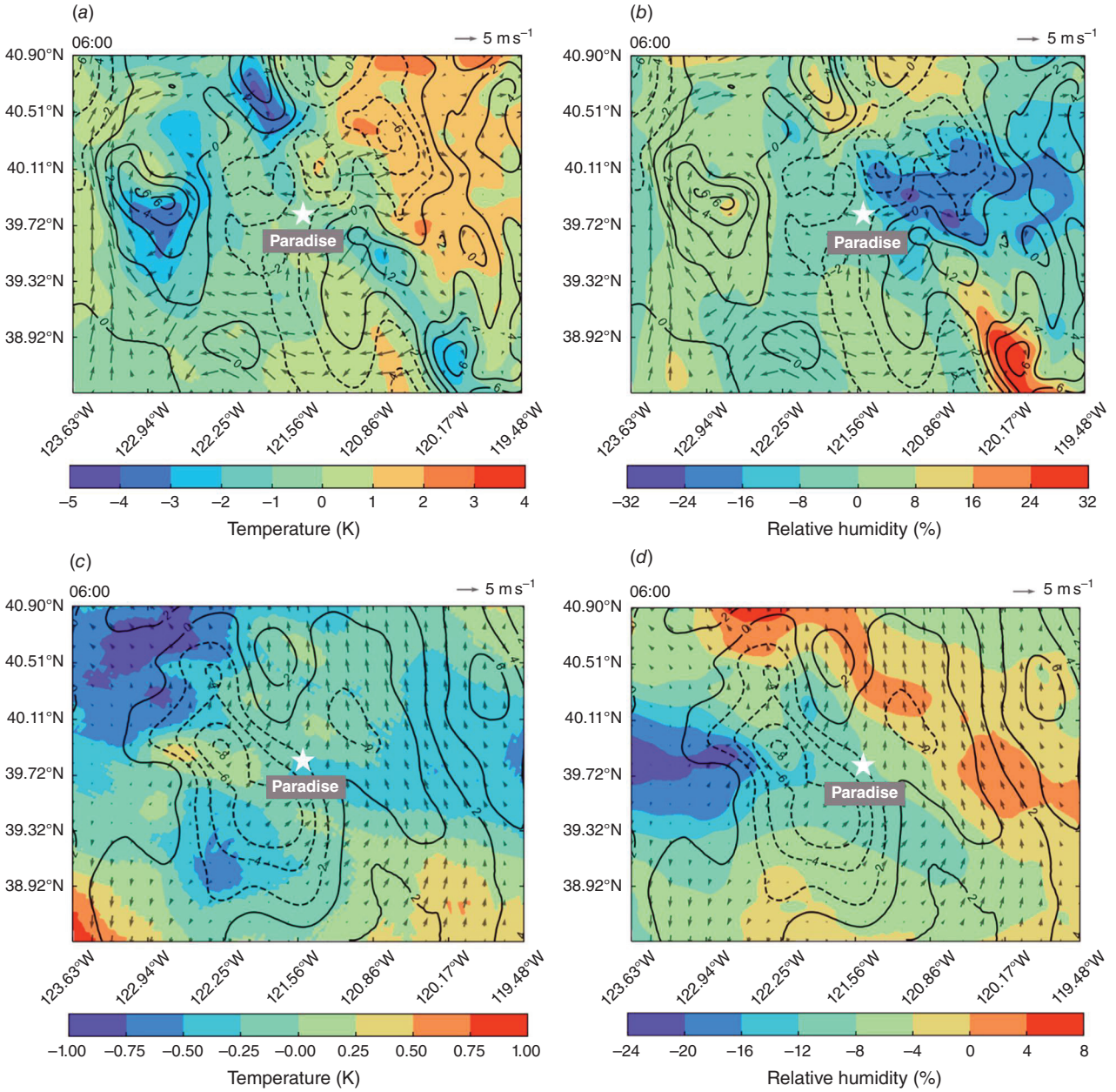

Fig. 9. Differences of the initial atmospheric state in the outermost domain of Weath1 (derived from ERA5 forcing) and Base (derived from HRRR forcing) cases. (*a*) Temperature and (*b*) relative humidity difference at 850 mb, and (*c*) temperature and (*d*) relative humidity difference at 500 mb pressure levels (1 mb = 100 Pa). Differences are calculated as Weath1 minus Base. Contours and arrows represent geopotential height difference (m) and wind field difference, respectively.

weaker northerly winds in the Weath1 case. In contrast, the wind speed on the east side of the Route 70 is similar in all cases. Furthermore, large terrain-induced eddies are apparent in Spin3 (Fig. 12*b*) and Spin6 (Fig. 12*c*) in the south-west and north-west parts of the domain.

The impacts of these spin-up induced wind differences on fire spread are summarised in Fig. 13. Notably, none of the spin-up tests yield a fire perimeter similar to the radar observations. Moreover, while the fire perimeter in all the cases is almost the same near the end of the simulation, the ROS decreases as the spin-up time increases at the beginning of the simulations. Moreover, the simulated fire still slows down at the Feather River canyon and stops at the West Feather River canyon. The reason is likely due to the relatively large grid resolution (i.e. 111 m) of the innermost atmospheric domain, which may result in poor representation of the terrain, especially on the east side of the domain, where the terrain is complex. Therefore, the innermost domain resolution is refined using the 3-domain setup to investigate the sensitivity of the model to atmospheric grid resolution.

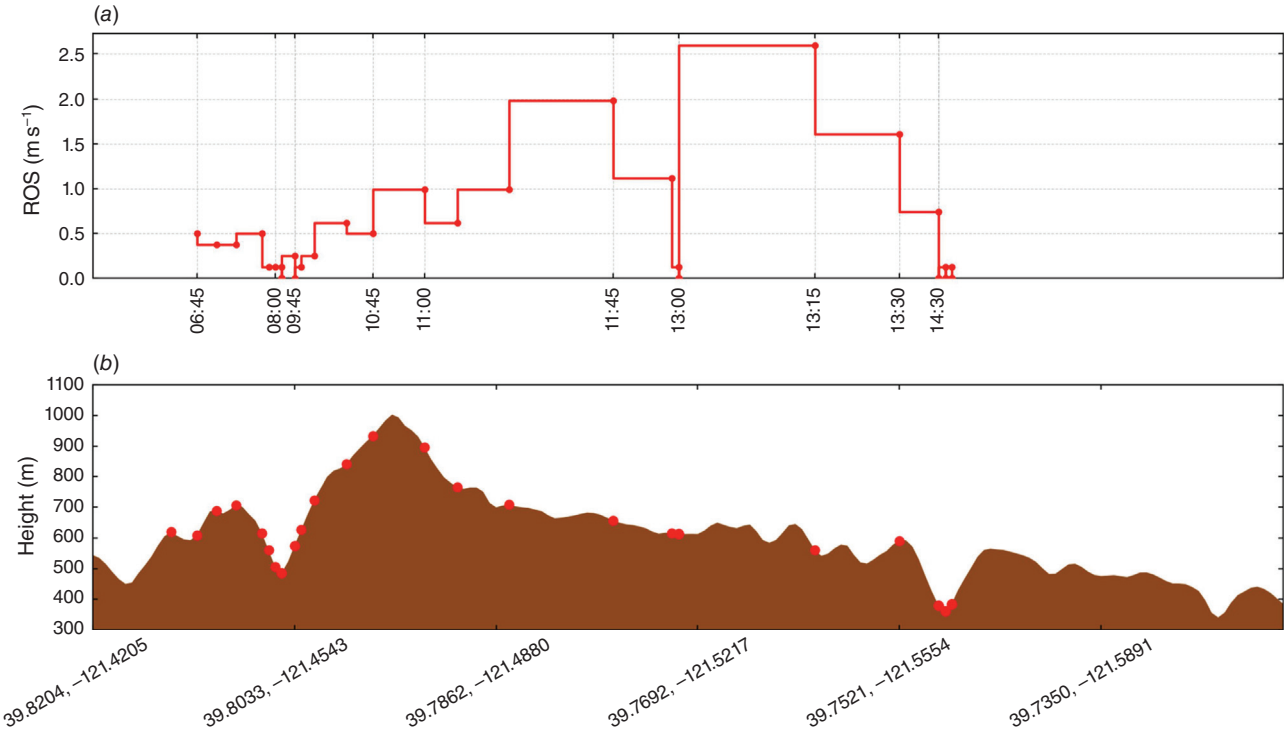

Fig. 10. Time history of the simulated fire head (*a*) ROS and (*b*) location along a–a cross-section in the Weath1 case. Red circles in both figures indicate the fire head, and brown shading shows the terrain.

Summary of 2-domain cases

Before moving to the 3-domain sensitivity simulations, and to better compare the simulated and observed fire behaviour in 2-domain cases, a similarity index (SI) is defined to measure how well the simulated and observed burned areas match at each time. SI varies from [0, 1], where 1 stands for a perfect match between the burned areas and 0 stands for no intersection between the burned areas.

$$\mathrm{SI} = \frac{\mathrm{area}(A \cap B)}{\mathrm{area}(A \cup B)} \tag{1}$$

where, A is the simulated burned area, and B is the observed burned area derived from radar observations. Moreover, the Burned Area Rate (BAR) is defined as follows to characterise the rate at which the fire is burning.

$$\mathrm{BAR} = \frac{\text{Fire area}_{t+1} - \text{Fire area}_t}{\Delta t} \tag{2}$$

in which fire areas are the total burned area at two consecutive time steps, and Δt is the time step size, which is 15 min in this study, same as WRF-Fire output interval.

The SI for all the 2-domain case studies is shown in Fig. 14*a* as a function of time. As seen in Fig. 14*a*, the maximum SI achieved is about 24% and belongs to the Weath1 case, while the baseline case has the lowest SI. Moreover, BAR for all the 2-domain simulations and radar-driven observations are shown in Fig. 14*b* as a function of time. The BAR in all simulations is lower than observations at the beginning of the simulation. The simulated BAR better matches the observations in the middle of the simulations, from 12:45 hours to 15:45 hours (PST). The simulated BAR decreases near the end of the simulations, whereas the radar-driven fire boundaries propagate at faster rates than the simulation from 16:00 hours to 16:45 hours (PST).

The SI and BAR criteria can conclude that while the simulated fire propagation process matches the observations to some extent, there are significant differences between real-world fire and WRF-Fire simulations of Camp Fire when the 2-domain setup with 111 m resolution in the innermost atmospheric domain is used.

Effects of atmospheric grid resolution

Representation of topography, especially in complex terrain, affects the simulated wind field by creating turbulence, mountain waves, and terrain-induced eddies, and thus, affects fire spread. In the previous cases, the 111 m resolution of the innermost atmospheric domain is roughly three times the available 30 m SRTM topography, meaning the topography is smoothed in the atmospheric model. This smoothing may degrade the model representation of the winds and turbulence. To test the impact of the grid (and thus terrain) resolution, the innermost domain resolution is refined to ~28 m. To achieve a smooth transition from 1 km outer domain to 28 m inner domain, a 3-domain case (3dom

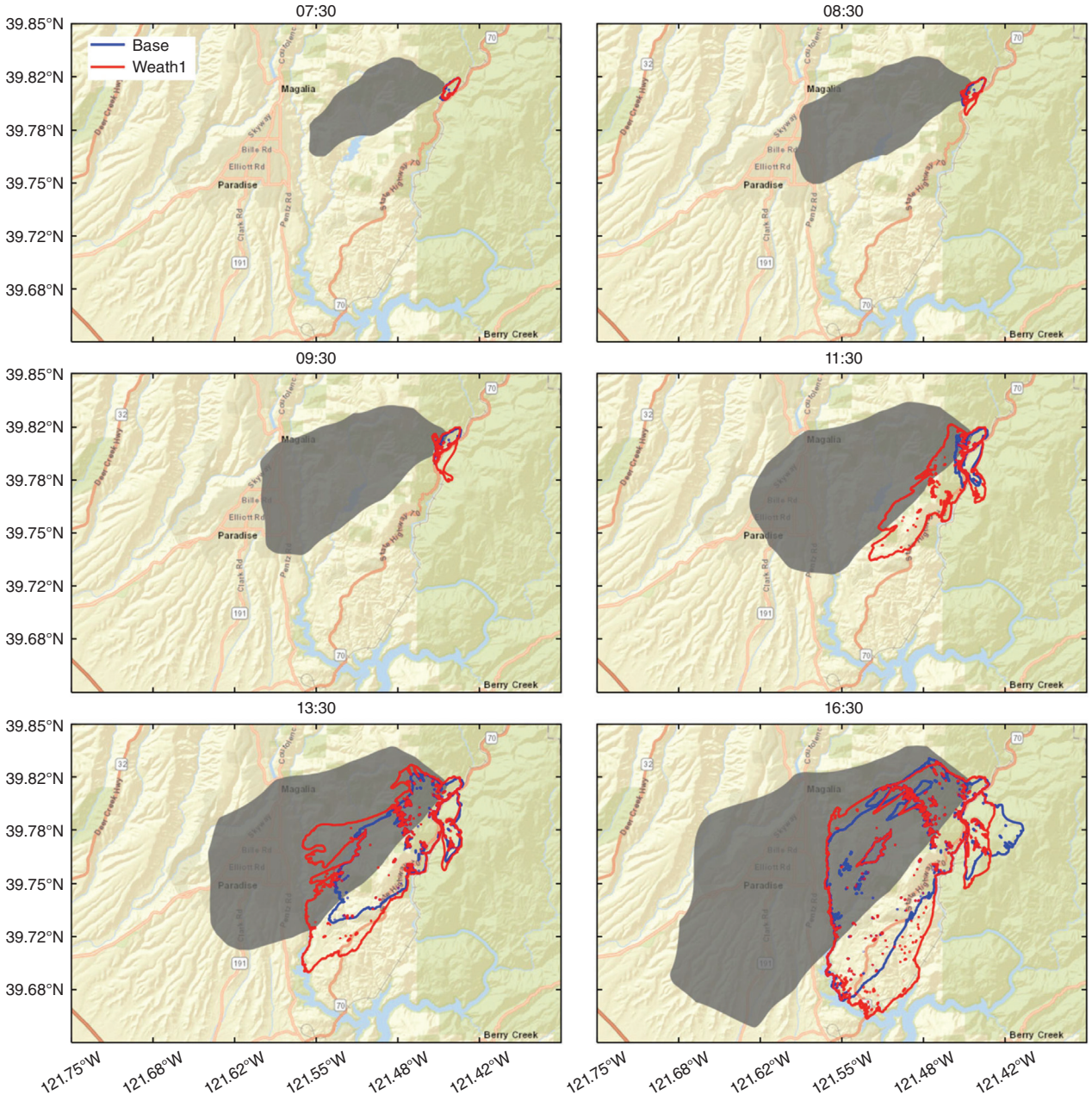

Fig. 11. Comparison of the snapshots of simulated fire perimeter for 2-domain case studies: baseline (blue line) and Weath1 (red line) case studies with radar-driven observed fire perimeter (grey shading). The abbreviations are based on Table 1, and the related PST time is indicated for each subplot.

in Table 1) is used with the middle domain at 111 m and the inner domain at 28 m (see Fig. 3*a* for domain setups).

Fig. 15 compares the snapshots of radar-driven observed fire perimeter with the simulated fire perimeter obtained from the baseline 3-domain case (3dom), 3-domain with 3 h of spin-up time (3domspin3), which will be discussed in the next section, and 2-domain case with ERA5 forcing model (Weath1), which was the best-performing 2-domain. When compared to the observations, the fire perimeter obtained from the 3dom case has a better overall agreement with the observations compared to the Weath1 case. Fig. 16 shows the time history of fire ROS for the 3dom case, showing a short 'stalling' at Feather River canyon (08:00–09:30 hours; PST) as compared to Weath1. The fire then propagates uphill with larger ROS than the Weath1 case reaching the maximum value of 1.9 m s^{-1}. After passing the summit, the fire quickly propagates downhill with average and maximum ROS of 2 and 3.2 m s^{-1}, respectively. The fire arrives at the West Feather River canyon at around 14:15 hours (PST), and it passes the canyon around 15:15 hours (PST).

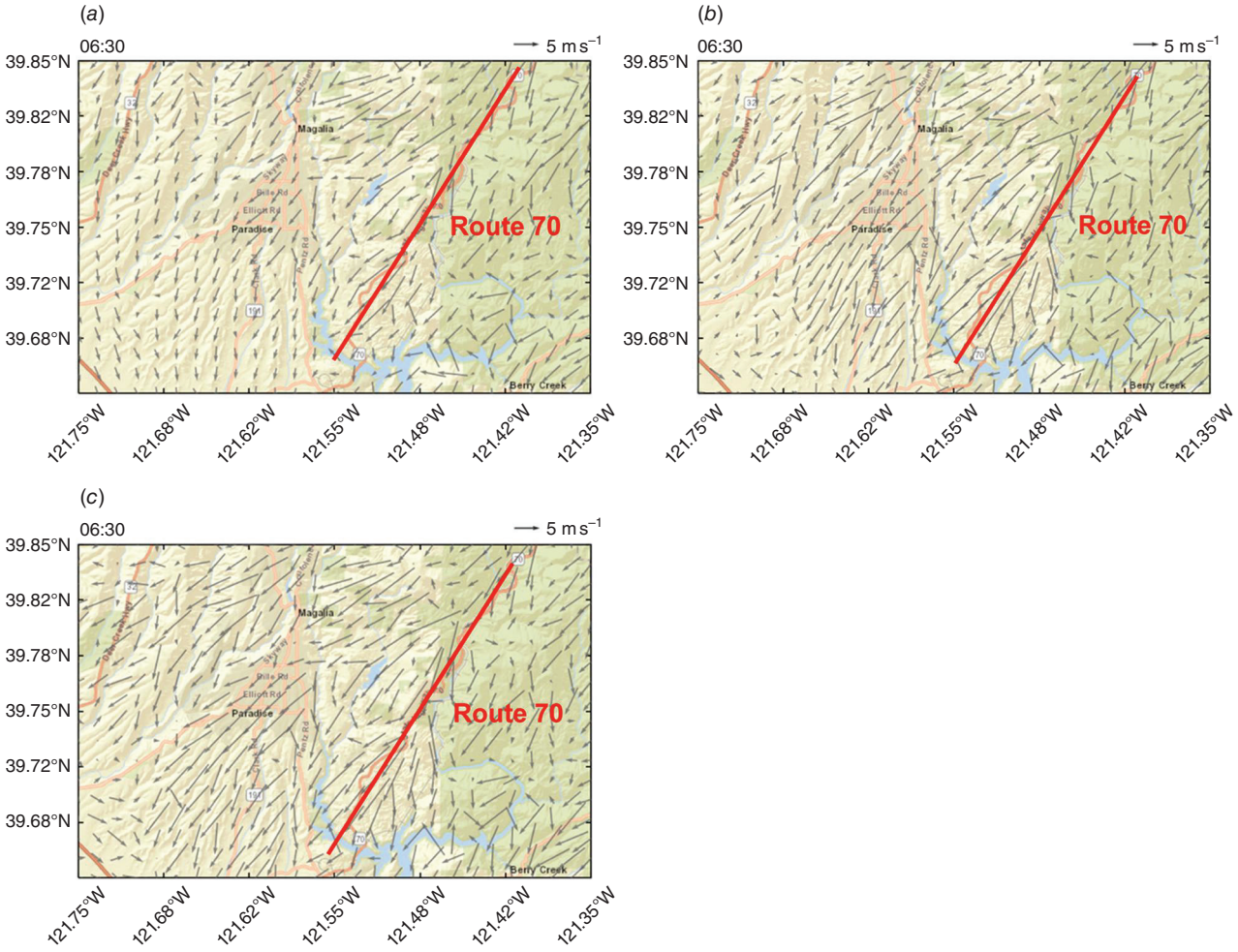

Fig. 12. Comparison of the simulated wind field at fire wind height in (*a*) Weath1, (*b*) Spin3, and (*c*) Spin6 case studies.

Finally, the fire reaches the Pentz road at around 16:45 hours (PST) and stops at the road. Though the fire in the 3dom and Weath1 reaches the same location at 11:30 hours (PST), the fire in the 3-dom case propagates with larger overall ROS and slows at both canyons for less time compared to the Weath1 case, resulting in better matching simulated and observed fire boundaries.

Furthermore, Fig. 17 shows the wind field at the two canyons in the 3dom case when the fire slows down in the canyons, which is the same as Fig. 8 plotted for the baseline case. The figure shows significant differences in both the wind speed and direction in the two canyons compared to Fig. 8. In the 3dom case, the wind direction is upslope (i.e. out of the canyon), contrasting with the downslope or along canyon wind seen in the baseline case. The wind speed is also higher in the 3dom case, which enables the fire to propagate uphill and pass both canyons. In general, it can be concluded that the model is highly sensitive to the topography, and refining the terrain representation results in an improved agreement between simulated and observed fire perimeters. To study the effects of a well-mixed boundary layer in the refined terrain, the effects of spin-up on the 3dom case are investigated in the next step.

Effects of spin-up time in 3-domain model

To allow WRF atmospheric model to resolve turbulent eddies and investigate the effects of a well-mixed boundary layer over refined topography on the fire propagation process, the 3-domain case, the 3dom model, is run with 3 h of spin-up time, which will be referred to as '3domspin3' this point forward (Table 1).

The wind fields at fire wind height (i.e. 6.5 m) prior to ignition for the 3-domain cases with 25 min and 3 h of spin-up time, 3dom and 3domspin3, are shown in Fig. 18. When compared to Fig. 12, Fig. 18 presents different wind fields in Spin3 and 3domspin3 cases prior to ignition. On the east of the Pentz road, the 3domspin3 case presents a larger wind speed than the Spin3 case, and wind direction is also different compared to the Spin3 case. Furthermore, the wind

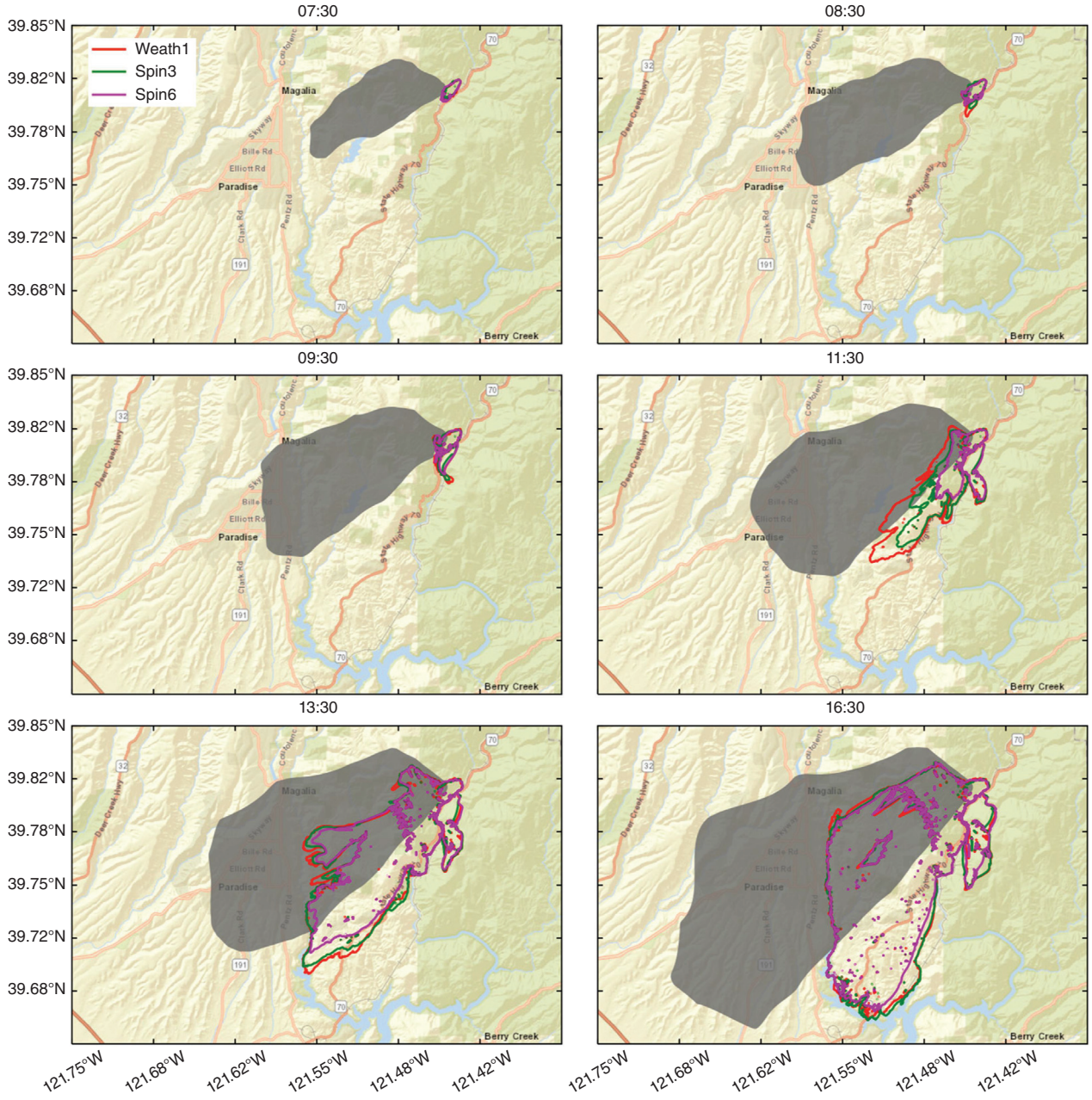

Fig. 13. Comparison of the snapshots of simulated fire perimeter for 2-domain case studies: Weath1 (red line), Spin3 (green line), and Spin6 (magenta line) case studies with radar-driven observed fire perimeter (grey shading). The abbreviations are based on Table 1, and the related PST time is indicated for each subplot.

speed in the 3domspin3 case is larger compared to the 3dom case in the inner domain, especially over and to the west of Paradise.

Comparing the simulated fire perimeter snapshots with the radar-driven perimeter presented in Fig. 15 indicates that the increased wind speed due to higher spin-up time resulted in increased fire ROS in the 3domspin3 case in contrast to the 3dom case, and it better matches the observations. Still, the overall fire propagation direction differs from the observation, and it is more southerly instead of westerly. This is likely due to the incorrect overall wind direction and probably related to the meteorological forcing model. Further investigation of the results shows that the fire fingers pass the Pentz road (Fig. 15), which indicates possible inaccuracies in the fuel map compared to the real world.

Inspecting the fire ROS time history and its location shown in Fig. 19 indicates that the fire reaches the Feather River canyon at around 07:45 hours (PST), and although it slows down at the canyon, it starts moving uphill at the next

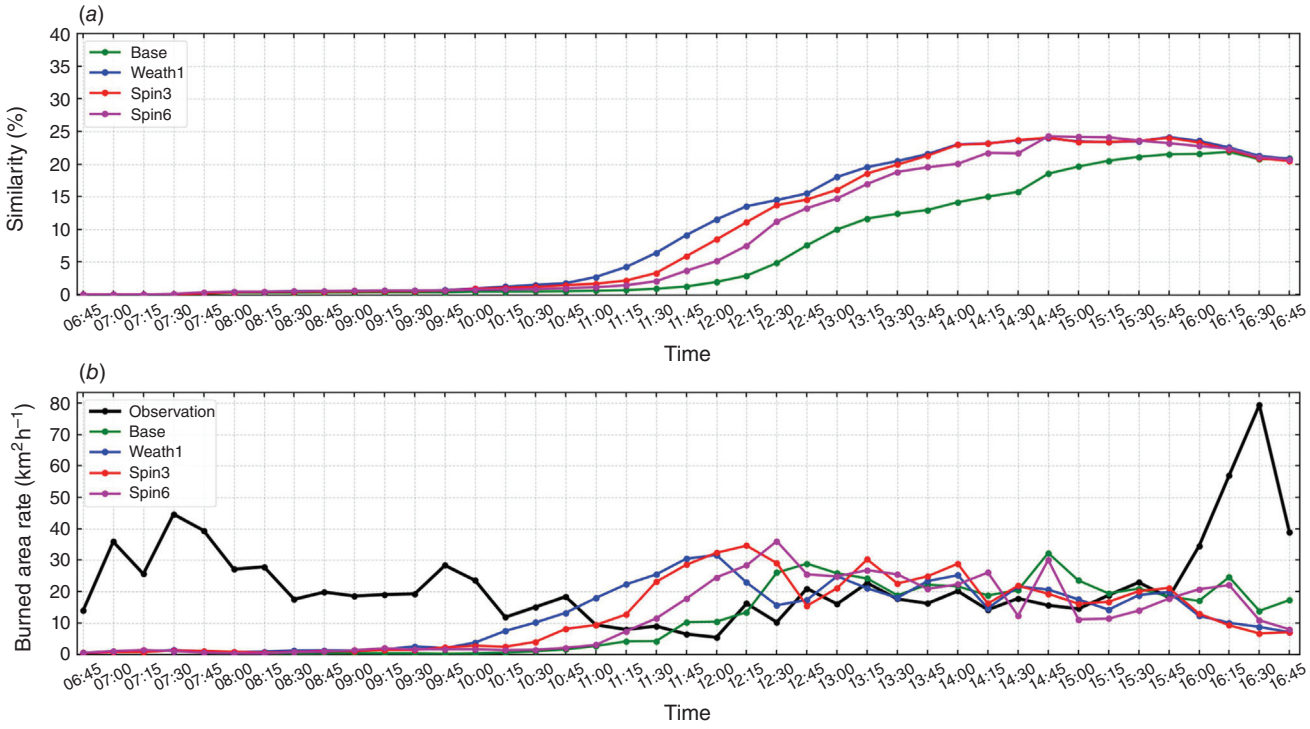

Fig. 14. (*a*) Similarity index (SI) between simulations and observations, and (*b*) fire burned area rate (BAR) in the 2-domain case studies. Abbreviations are based on Table 1.

output interval, which is 08:00 hours (PST). The fire propagates with a relatively high ROS compared to all the previous simulations until it passes the summit between 09:15 hours and 09:30 hours (PST), and it propagates with a maximum ROS of about 3.5 m s^{-1} until it reaches the West Feather River canyon at around 11:45 hours (PST), where it slows down until 14:30 hours (PST). After passing the second canyon, the fire continues propagating with a large ROS, reaching 4.5 m s^{-1} toward the end of the simulation. In summary, the 3domspin3 case clearly indicates the effects and the importance of properly representing the topography and allowing the atmospheric model to resolve the terrain in the Camp Fire simulation.

Summary of 3-domain cases

The SI and BAR defined in equations (1) and (2) are calculated for the 3-domain cases and shown in Fig. 20*a*, *b*, respectively. Fig. 20*a* shows that while the simulated fire in 3dom and 3domspin3 cases propagates at slower ROS than observation and SI is small at the beginning of the simulation; these cases have higher SI with the maximum value of 36% compared to the best 2-domain case, which is Weath1. Moreover, the SI of 3dom and 3domspin3 cases remain higher than Weath1 throughout the simulation. When comparing SI in 3dom and 3domspin3 cases, the 3domspin3 case, in general, have higher SI compared to the 3dom case. However, SI decreases in the 3domspin3 case between 12:15 hours and 14:45 hours (PST), which shows that even though the ROS is in better agreement with the observations for this case, the southward lateral propagation of fire is causing the overall fire perimeter to be less similar to the observations.

Fig. 20*b*, which shows BAR for 3dom and 3domspin3 cases, indicates that BAR is lower than the radar-driven observed fire at the first few hours of the simulations, same as the 2-domain cases. However, it is in good agreement with the observations from 09:00 hours–10:15 hours (PST) to 15:30 hours–16:00 hours (PST) in 3dom and 3domspin3 cases, respectively. Setting aside the fire perimeter that propagates more to the south-west compared to observations, the 3domspin3 case better represents the real-world fire beginning at 09:00 hours (PST) toward the end of the simulation in terms of BAR. Moreover, the 3domspin3 can predict the time of fire arrival into Paradise correctly, indicating a success metric for this model even though fire spotting is not accounted for.

Comparison of WRF-simulated wind field with RAWS

Validation of the simulated wind field is one of the key aspects of wildland fire simulation as wind is among the main drivers of the fire propagation process. However, this

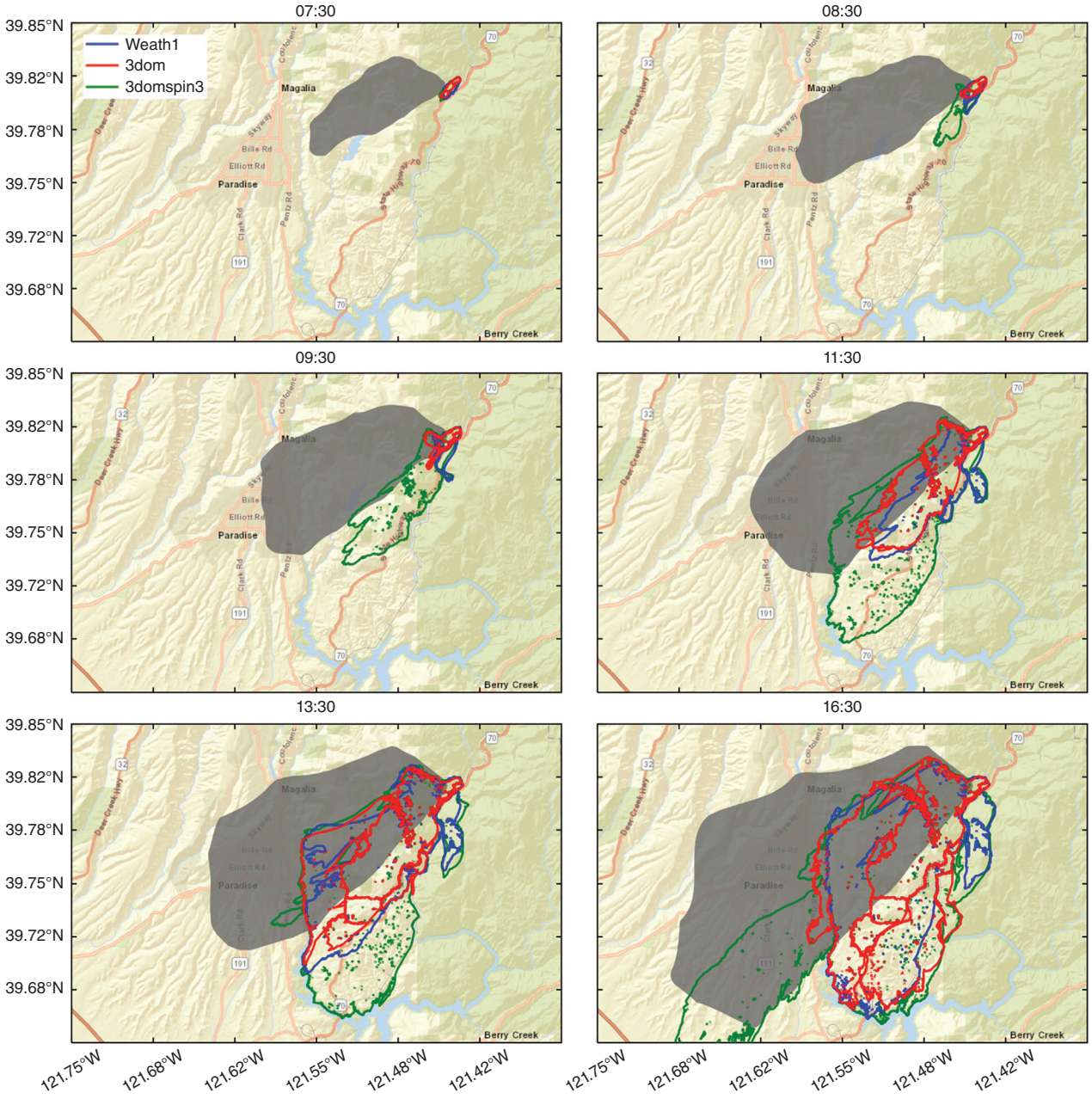

Fig. 15. Comparison of the snapshots of simulated fire perimeter for Weath1 (blue line), 3dom (red line), and 3domspin3 (green line) case studies with radar-driven observed fire perimeter. The abbreviations are based on Table 1, and the related PST time is indicated for each subplot.

requires comprehensive real-world observations such as several RAWS data. In the Camp Fire simulation, only one RAWS, Jarbo Gap, is located in the inner LES domain, which cannot lead into comprehensive validation of the fine-scale simulated wind field. Furthermore, several RAWS are located in the outer domain with which comparing the simulated wind field can validate the performance of the outer domain that feeds the inner domain. In this section, comparison of the simulated wind field of the outer and inner domains with the RAWS are presented. The names of the RAWS along with their abbreviation and their respective location to the simulation domains are presented in Table 2.

Fig. 21 compares the simulated wind speed and direction with observed wind speed, gust speed, and wind direction captured by the RAWS located in the outer domain of the Camp Fire simulation (as indicated in Table 2). The figure shows that the simulated wind speed and direction have reasonable match with all the RAWS observation with the simulated wind speed generally overestimated compared to the observed wind speed. This is in agreement with Brewer and

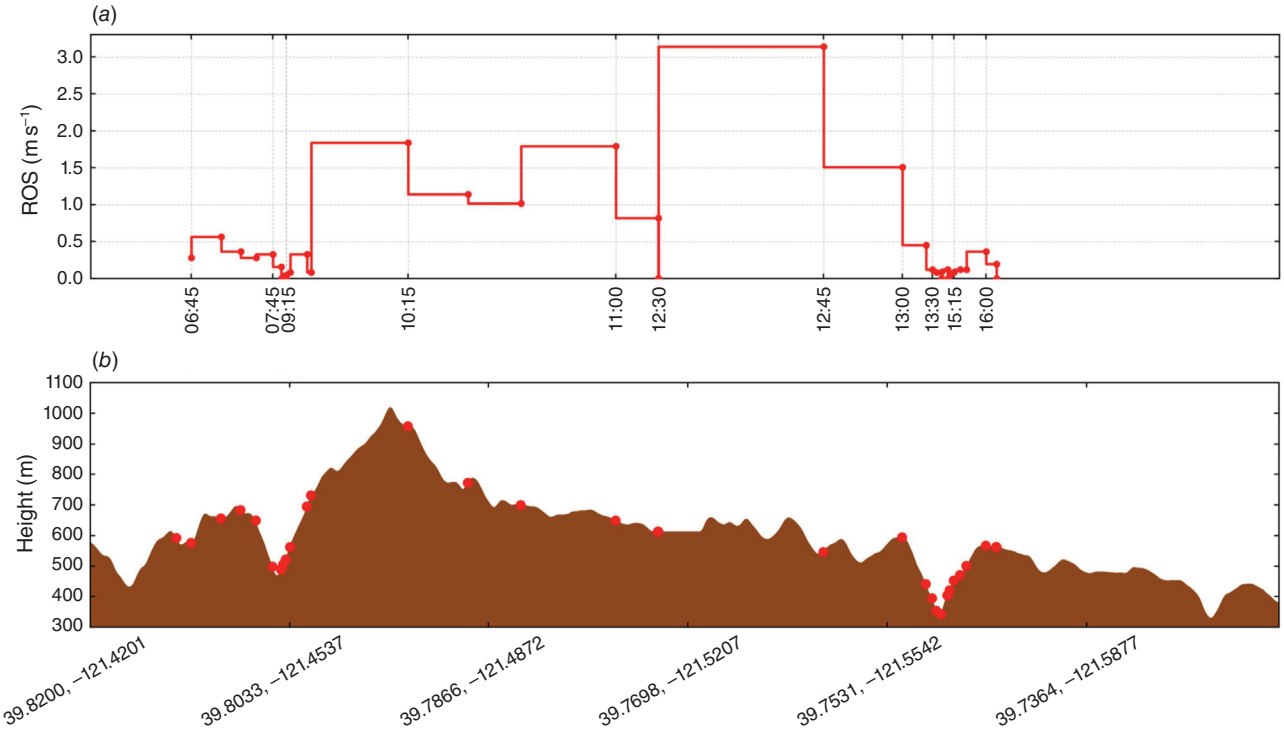

Fig. 16. Time history of the simulated fire head (*a*) ROS and (*b*) location along a–a cross-section in the 3dom case. Red circles in both figures indicate the fire head, and brown shading shows the terrain.

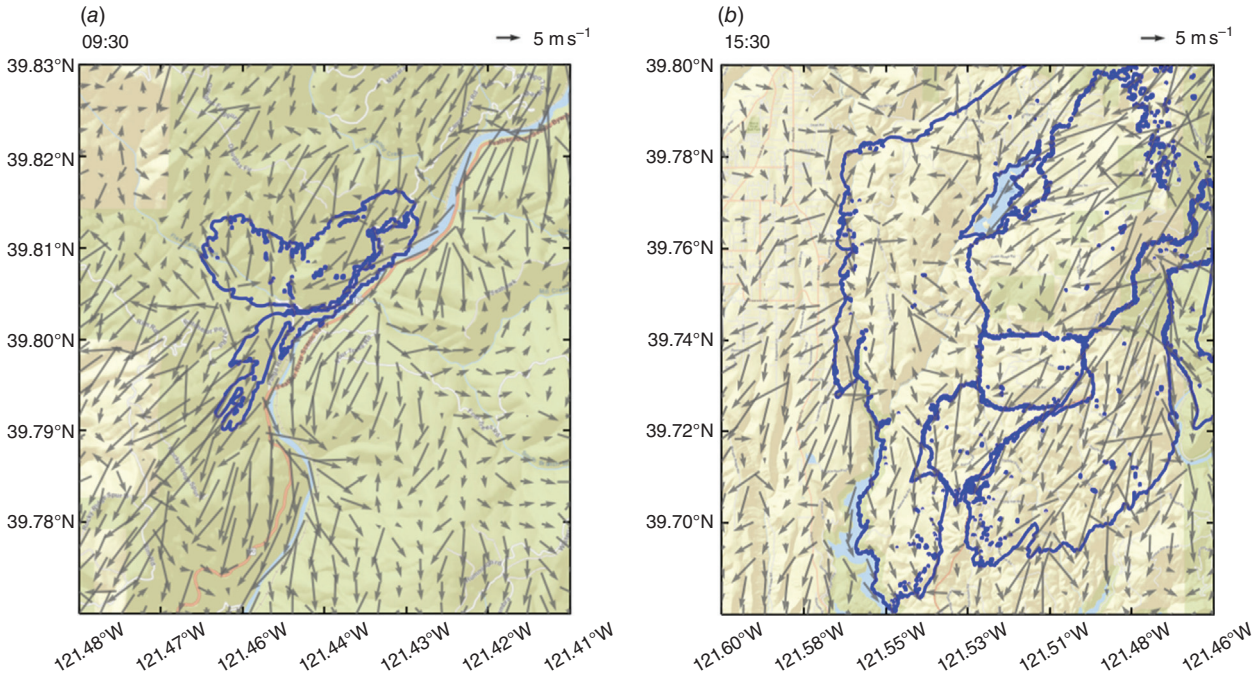

Fig. 17. The simulated wind field at (*a*) Feather River and (*b*) West Feather River canyons in the Camp Fire 3dom model.

Clements (2020) that presented overestimation of wind speed by WRF using mesoscale domain during Camp Fire event.

Furthermore, the simulated wind speed and direction of the inner domain is compared with JBGC1 RAWS, the only RAWS located in the inner domain, in Fig. 22. The simulated wind speed in the 2-domain cases is in reasonable agreement with the observed wind speed, whereas in the 3-domain cases, wind speed is between the observed wind

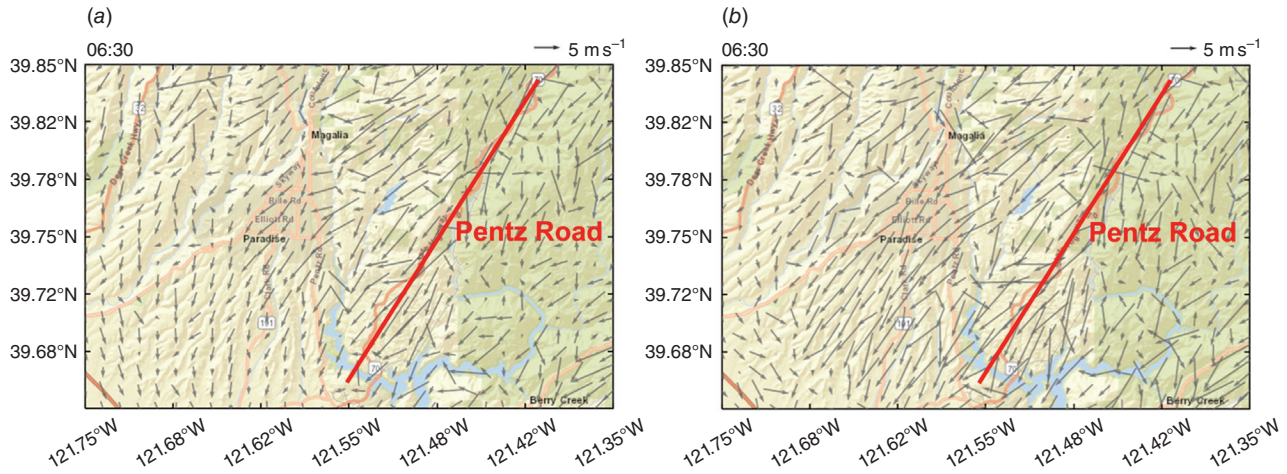

Fig. 18. Comparison of the simulated wind field at fire wind height in (*a*) 3dom and (*b*) 3domspin3 cases.

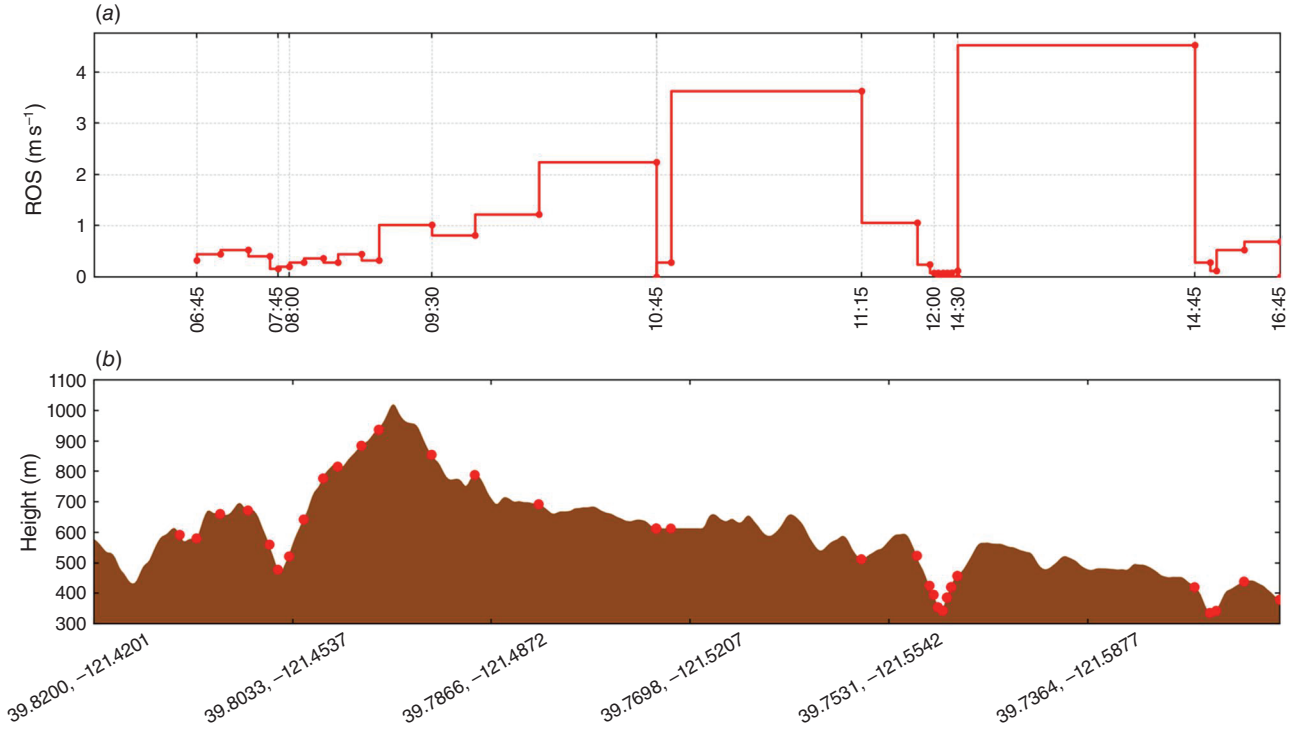

Fig. 19. Time history of the simulated fire head (*a*) ROS and (*b*) location along a–a cross-section in 3domspin3 case. Red circles in both figures indicate the fire head, and brown shading shows the terrain.

and gust speed (Fig. 22*a*). The discrepancy in the 3-domain cases with the observations increases between 14:00 hours and 15:30 hours (PST), where the simulated wind speed is ~2–4 m s^{-1} larger than the observed gust speed. In terms of the wind direction (Fig. 22*b*), all the cases present ~10–30 degrees discrepancy resulting in more north-easterly simulated wind compared to the observations. This can be the likely source of the incorrect spread direction in all the cases of this study. However, the comparison with only a single RAWS is not conclusive and highlights the need for high-resolution RAWS data to improve the future of wildland fire simulation capabilities.

Comparison of WRF-Fire and FARSITE for Camp Fire simulation

Comparing WRF-Fire results as a coupled fire-atmosphere wildfire propagation model with currently used uncoupled models such as FARSITE (Finney 1998) can provide insights into the

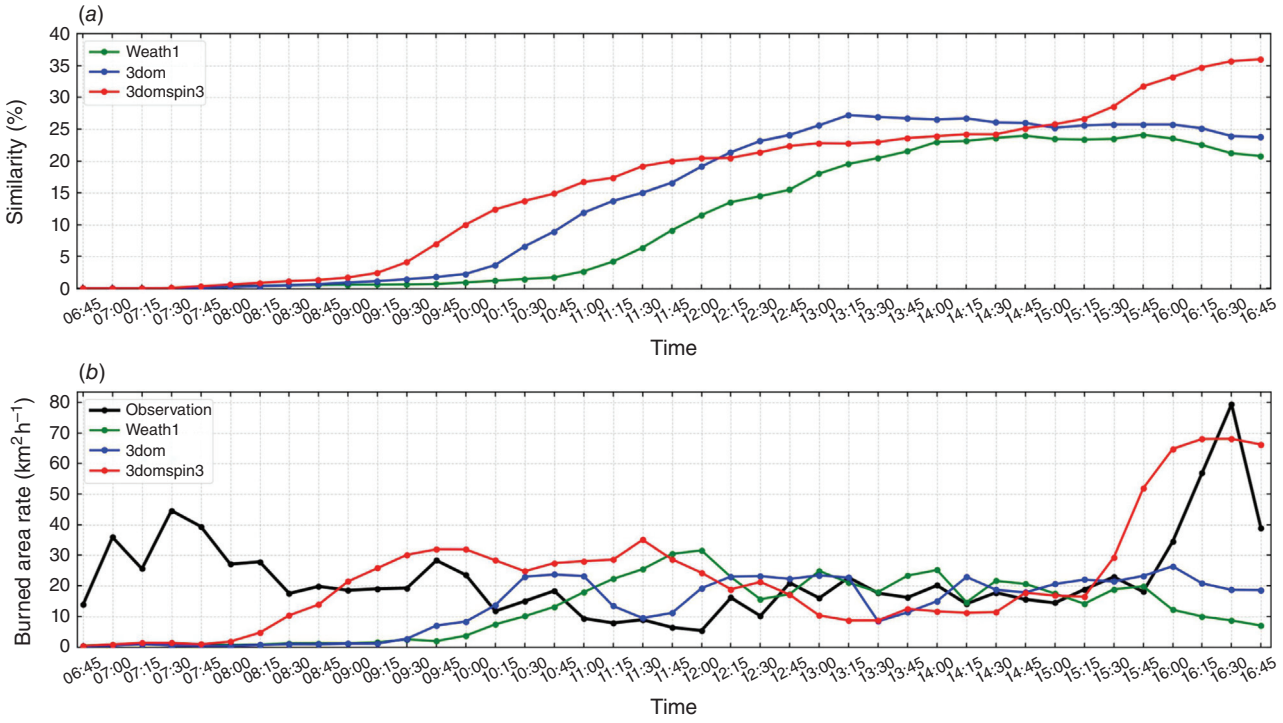

Fig. 20. (*a*) Similarity index (SI) between simulations and observations, and (*b*) fire burned area rate (BAR) in the 3-domain case studies. Abbreviations are based on Table 1.

Table 2. Remote Automatic Weather Stations (RAWS) used to validate the simulated wind field in Camp Fire simulation and their respective location to the simulation domains.

RAWS	Abbreviation	Outer 1 km domain	Inner 111 m/28 m domain
Chester	CESC1	Yes	No
Cashman	CHAC1	Yes	No
Colby Mountain	CBXC1	Yes	No
Swain Mountain	SWNC1	Yes	No
Jarbo Gap	JBGC1	Yes	Yes
Humbug Summit	HMRC1	Yes	No

effects and importance of fire-atmosphere coupling in wildfire simulation. Heat flux generated from fire results in updrafts and creates fire-induced circulations affecting the fire propagation. Furthermore, the atmosphere states, such as wind speed and direction, relative humidity, and temperature, are constantly changing both temporally and spatially. Therefore, the existence of an atmospheric simulation model, such as WRF within WRF-Fire, can provide temporally and spatially high-resolution weather data for wildfire simulation. In this section, WRF-Fire results for Camp Fire are compared to FARSITE, which is an uncoupled wildland fire simulation model.

FARSITE is based on Reothermel's ROS equation, the same as WRF-Fire, and it propagates the fire on the surface using Huygen's wave principle (Finney 1998). FARSITE is a widely used operational wildfire simulation platform in the U.S., and it is deemed the most accurate operational wildfire simulation model in literature (Sullivan 2009; Papadopoulos and Pavlidou 2011). FARSITE uses a detailed description of land features (including topography, vegetation type, crown height, etc.) and it uses user-defined constant atmospheric conditions.

FARSITE model setup for Camp Fire

The models used to simulate Camp Fire in FARSITE are similar to the 3-domain WRF-Fire model setup outlined in the Model setup. The land features are indicated using landscape files provided by the 2014 LANDFIRE database, and fuels are based on Scott and Burgan's 40 fuel categories. Input weather data – including wind speed and direction, relative humidity, and temperature – are provided at 60-min intervals based on the ERA5 weather prediction model. The horizontal grid resolution is set to 30 m. To simulate the spatial variation of the wind field, Windninja (Forthofer *et al.* 2014) is activated with a 30 m grid resolution. Two FARSITE models with and without crown fire and fire spotting are considered to investigate the effects of these features in FARSITE simulation results, and they will be referred to as 'FARCRSP' and 'FARBase' in the following sub-sections, respectively.

FARSITE results

The fire perimeter snapshots of FARSITE FARBase and FARCRSP, WRF-Fire 3domspin3 model, and real-world fire

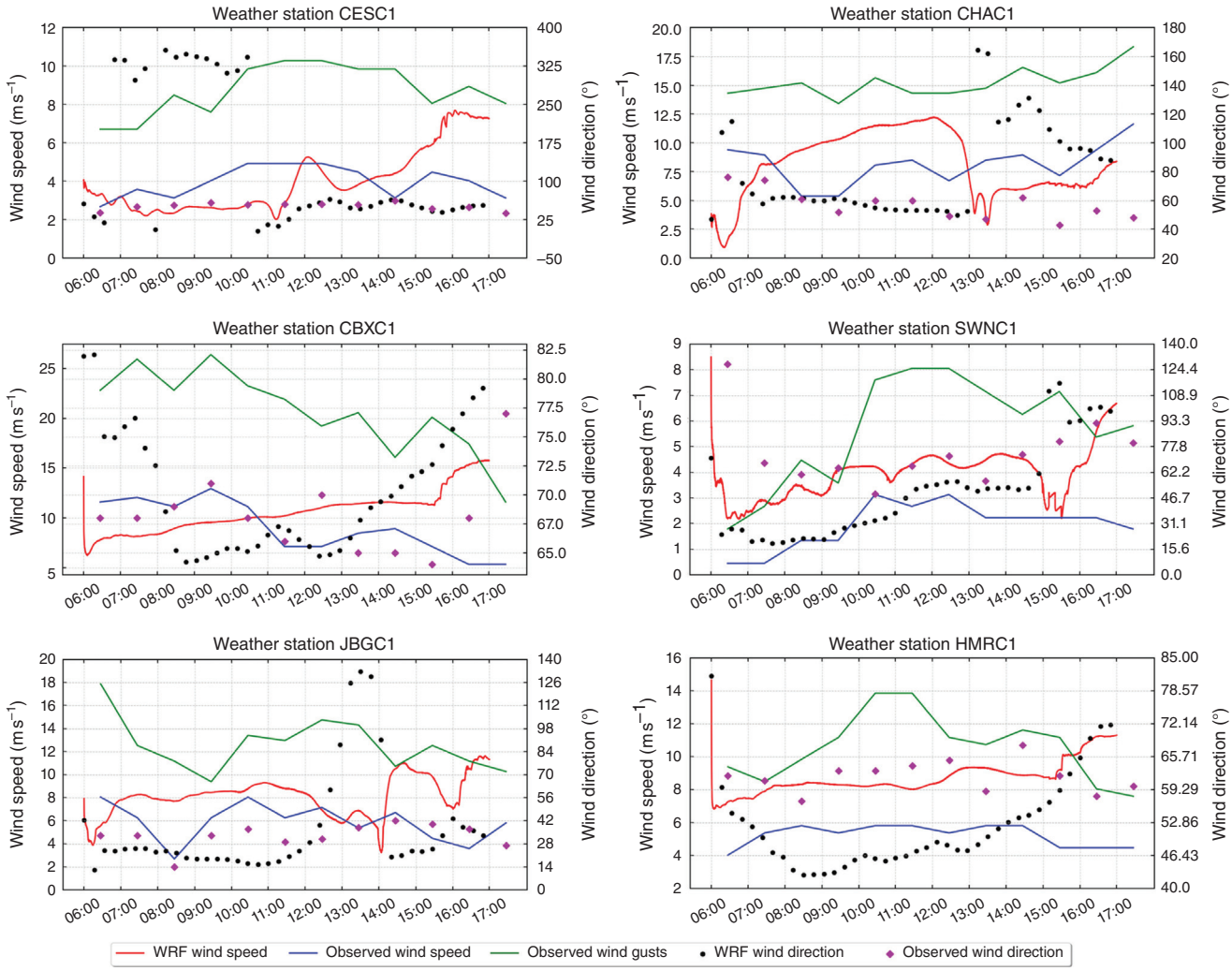

Fig. 21. Comparison of WRF simulated wind speed and direction with observed wind speed, gusts speed, and wind direction by RAWS located in the outer domain of Camp Fire simulation. Abbreviations are based on Table 2.

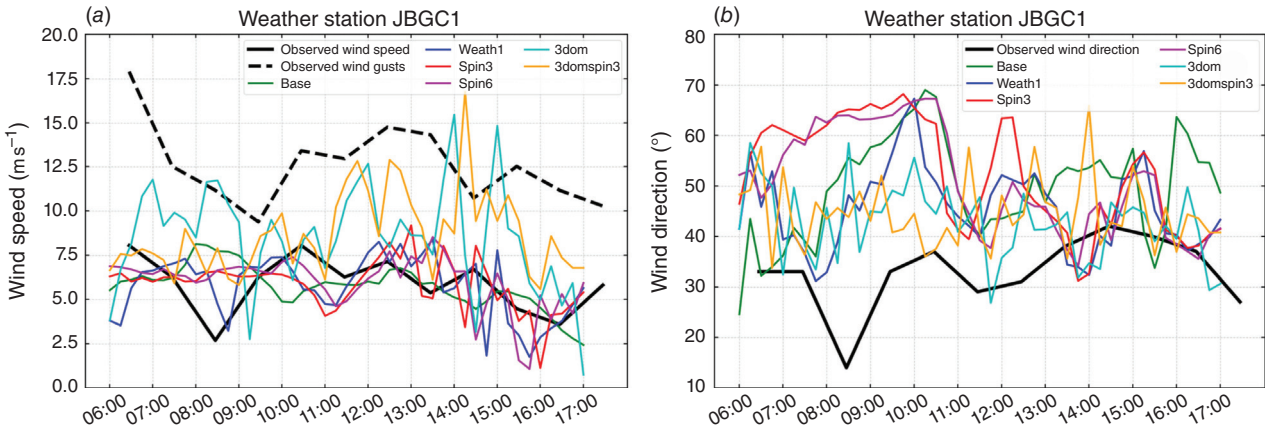

Fig. 22. Comparison of WRF simulated wind speed and direction with (*a*) observed wind and gusts speed, and (*b*) wind direction by JBGC1 RAWS located in the inner domain of Camp Fire simulation. Abbreviations for case studies and RAWS are based on Tables 1, 2, respectively.

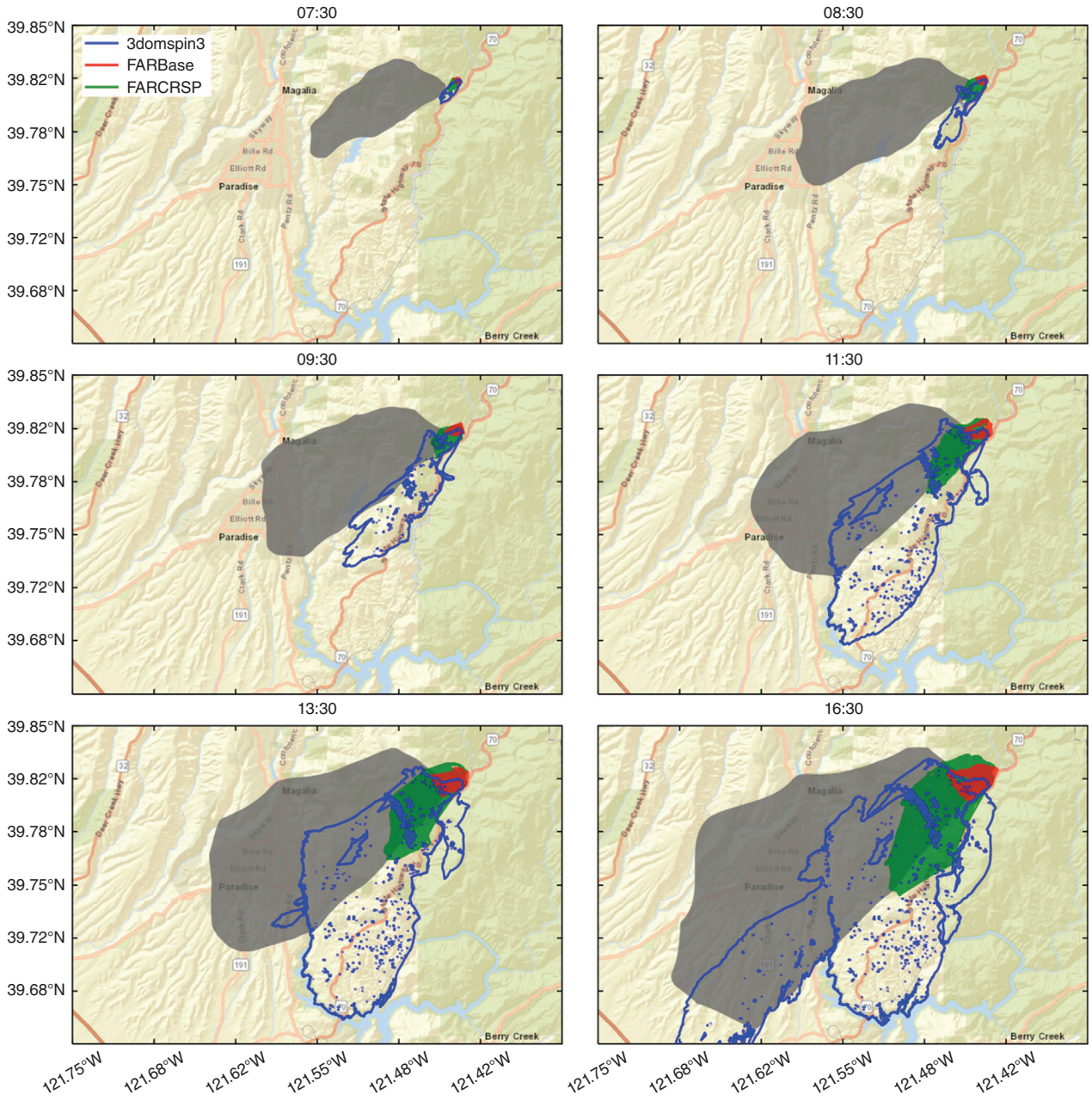

Fig. 23. Comparison of the snapshots of simulated fire perimeter for WRF-Fire 3domspin3 (blue line) and FARSITE 'FARBase' (red shading) and 'FARCRSP' (green shading) case studies with radar-driven fire perimeter (grey shading). The related PST time is indicated for each subplot.

are shown in Fig. 23. This figure shows that both FARSITE models are propagating at significantly lower ROS compared to the WRF-Fire 3domspin3 simulation results and the observations. In terms of spread direction, the FARSITE models better match the observations, but they lack northerly lateral propagation. In contrast, the WRF-Fire 3domspin3 simulated boundary has a northerly lateral propagation, which helps the fire perimeter to better match the observations. A comparison of the FARBase and FARCRSP shows that crown fire and fire spotting features increase the fire ROS and result in a better match with real-world fire boundaries. This can demonstrate the importance of crown fire and fire spotting to simulate wildland fire and can pinpoint the need to implement these features in WRF-Fire.

Fig. 24 presents SI and BAR for FARSITE FARBase and FARCRSP models together with the WRF-Fire 3dom model. Investigating SI in the figure shows that all the three models have almost identical low similarity with the observations until 10:00 hours (PST). After 10:00 hours (PST) until the

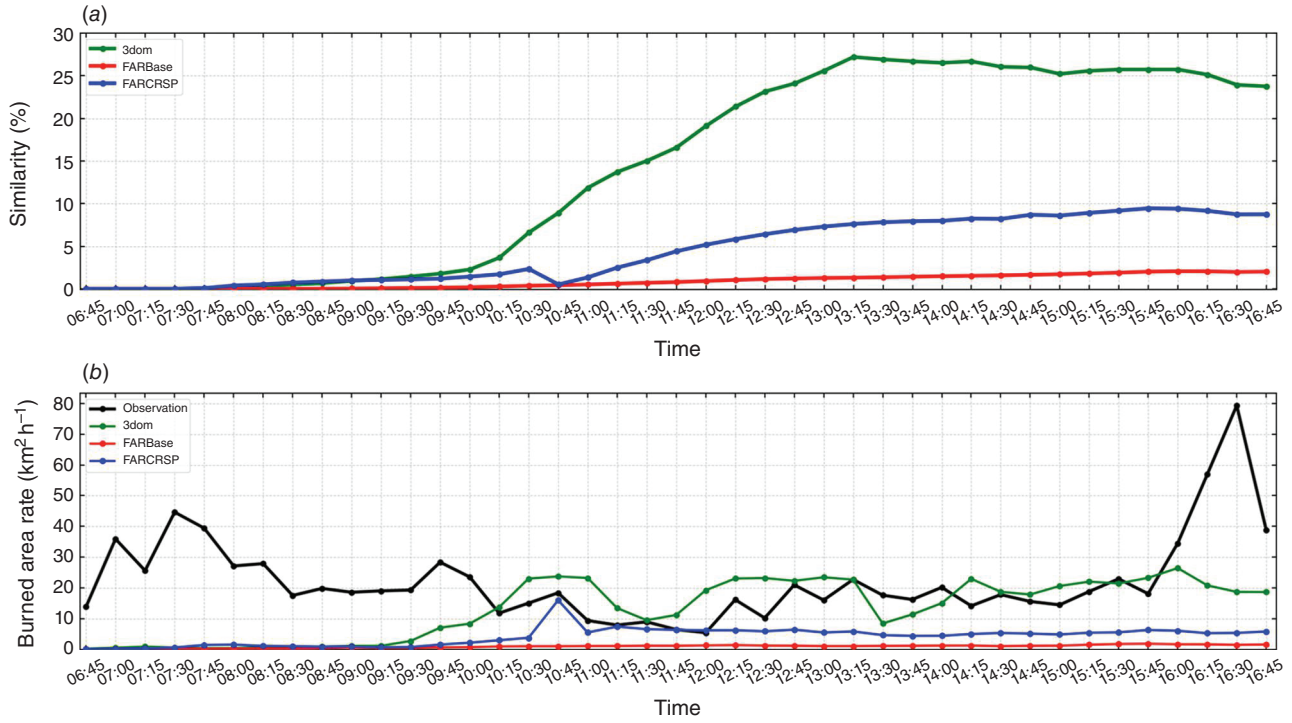

Fig. 24. (*a*) Similarity index (SI) between simulations and observations, and (*b*) fire burned area rate (BAR) in WRF-Fire 3dom and FARSITE case studies of Camp Fire.

end of the simulation, the WRF-Fire 3dom case has the highest similarity (maximum of ~27%) with the observations among all the three cases, followed by FARCRSP (maximum of ~10%) and FARBase (maximum of ~3%). Moreover, BAR in the figure shows a similar pattern as SI for the three cases. WRF-Fire 3dom case has the highest BAR, while FARCRSP and FARBase have the middle and lowest BAR in all the cases. Compared to the observations, WRF-Fire 3dom has a relatively better agreement with the observations than the two FARSITE models.

Considering both WRF-Fire and FARSITE models use the same fire ROS theory (i.e. Rothermel model) and fuel data, the non-negligible differences between the two simulation models highlight the effects and the importance of: (1) fire-atmosphere coupling to allow the fire to 'create its own weather'; and (2) temporally and spatially high-resolution atmospheric data to account for the weather changes, two important factors that can increase the simulation agreement with real-world fire behaviour.

Computational demand

All the WRF-Fire simulations of Camp Fire were run on National Center for Atmospheric Research (NCAR)'s Cheyenne supercomputer that includes 36 × Intel Xeon E5-2697V4 CPU cores per node. The computational demand of 2-domain and 3-domain configurations of Camp Fire are presented in Table 3. It should be noted that the purpose of this study is not operational simulation and hence, the scalability of the models is not thoroughly investigated. The wall-clock and CPU time ratios in Table 3 is equal to the required wall-clock and CPU time, respectively, divided by the simulation time (e.g. wall-clock time ratio of eight means 1 h of simulation requires 8 h of wall-clock time). Since only the horizontal grid resolution affects the computational demand of WRF-Fire from the parameters investigated in the sensitivity analysis, the computational demand of WRF-Fire is presented for 2- and 3-domains cases in the table.

Table 3. Computational demand of WRF-Fire in Camp Fire simulation using Cheyenne HPC.

Model setup	No. nodes	No. CPUs	Wall-clock time ratio	CPU time ratio
2-domain	16	576	1	576
3-domain	16	576	7.7	4435

The FARSITE simulations of Camp Fire were run on a desktop computer with Intel Xeon Gold 6130 CPU, though FARSITE only uses one core for the simulations. Table 4 presents the computational demand of FARSITE Camp Fire models. The table shows that adding crown fire and spotting simulation to the FARSITE model in the FARCRSP case increases the computational demand by a factor of five compared to the FARBase case.

Table 4. Computational demand of FARSITE in Camp Fire simulation using a desktop computer.

Model setup	No. CPUs	Wall-clock time ratio	CPU time ratio
FARBase	1	0.023	0.023
FARCRSP	1	0.13	0.13

Discussion

The discrepancies between the simulated and the observed fire boundaries in all the cases can be due to modelling uncertainties and errors, which can stem from: (1) inaccurate atmospheric forcing model; (2) inaccurate ignition location; (3) lack of spotting in the model; (4) inaccurate high-resolution, microscale wind field; and (5) inaccurate fuel map and/or model. As mentioned in the Camp Fire section, the ignition location is uncertain as the fire was first reported by a 911 emergency call. Lack of the ability to simulate fire spotting in WRF-Fire will likely result in slower ROS as spotting was one of the key drivers of the Camp Fire spread (Maranghides *et al.* 2021). The wind speed and direction, key parameters controlling the fire propagation, can affect both the fire ROS and spread direction. Consequently, simulating the wind field more accurately can result in more accurate fire propagation. Fuel is another key factor driving wildfire, and an inaccurate fuel map and/or fuel model can result in different fire propagation processes and time histories.

This study had a number of limitations. Lack of diverse observational datasets during the event limited our ability to evaluate different aspects of the simulation results. For instance, real-world observations of weather, such as wind speed and direction near the fire perimeter, could have been useful to comprehensively assess WRF-Fire performance in simulating the underlying atmospheric conditions. Moreover, although the focus of this study was on atmospheric modelling effects, other possible sources of modelling uncertainties and errors must be investigated in a systematic way to achieve a thorough understanding of WRF-Fire performance and best modelling practices. Future efforts are underway to repeat similar studies for other major wildland fires to gain more insight into WRF-Fire best modelling practices.

Summary and conclusions

This study assessed the performance of WRF-Fire, a fully coupled fire-atmosphere wildland fire simulation platform, in simulating the 2018 Camp Fire by comparing the simulated and radar-driven fire perimeters. A sensitivity analysis was performed on a number of modelling parameters and assumptions to examine WRF-Fire performance and limitations. We started simulating Camp Fire using a baseline setup typically used for operational wildfire simulation by Colorado Fire Prediction System (CO-FPS) (Jiménez *et al.* 2018*a*). A comparison of the results showed non-negligible differences between the simulations and observations in terms of fire ROS and direction. The simulated fire propagated at much slower ROS and in the wrong direction compared to the observations. Furthermore, the simulated fire slowed down at Feather River and West Feather River canyons in contrast to the radar-driven fire perimeters. The similarity between the simulated and observed fire perimeters was measured using a SI, which is defined as the ratio of the intersection of the simulated and observed fire areas divided by their union. The SI index in the baseline case did not exceed 20%, which showed a low similarity between the simulated fire and the observations.

The sensitivity analysis was focused on a number of modelling parameters and assumptions governing the simulated wind field. The sensitivity analysis included the effects of: (1) atmospheric forcing model; (2) spin-up time; (3) refining atmospheric grid; and (4) spin-up time in the refined domain. To study the effects of the atmospheric forcing model on the baseline case, we compared the simulation results of two models whose initial and lateral boundary conditions were derived using the HRRR and ERA5 forcing models. The simulated fire of the model that used ERA5 propagated with higher ROS and slowed down at the first canyon for a shorter period compared to the baseline case resulting in better agreement with the observations. Hence, we used the ERA5 forcing model in the other case studies.

For the effects of spin-up time, the spin-up time was increased from 25 min to 3 and 6 h. The results showed that the simulated fire ROS decreased as the spin-up increased. In the next step, we refined the atmospheric grid resolution by a factor of three to investigate the effects of horizontal atmospheric grid resolution. The results of this case were in better agreement with the observations compared to all the previous cases in terms of fire ROS, with SI increasing to about 27%. Next, the spin-up time of the model with a refined atmospheric domain was increased from 25 min to 3 h. The increased spin-up time resulted in the simulated fire propagating with ROS almost equal to the observations, and SI reached 35% near the end of the simulation. This clearly showed the importance of properly representing the topography and allowing the model to resolve terrain-induced circulations and turbulence, such as mountain waves, in complex terrains.

The simulated wind field in this study was compared with several RAWS data in the outer domain as well as Jarbo Gap (JBGC1) RAWS data in the inner LES domain. While showing overestimations in the simulated wind speed, the comparison showed that the simulated wind speed and direction in the outer domain were in reasonable agreement with the RAWS data. The inner domain, however, performed better than the outer domain when compared to the JBGC1 station in terms of the wind speed, whereas discrepancies with the data were observed for the wind direction.

Comparison of WRF-Fire with FARSITE, which is a widely-used operational uncoupled wildfire simulation

model, showed non-negligible differences. The simulated fire from the FARSITE model with crown fire and spotting activated, the features that were not used in WRF-Fire simulations, were in less agreement with the observations compared to WRF-Fire simulations. This showed the importance of considering fire-atmosphere coupling in complex-terrain fires such as the Camp Fire.

References

Abatzoglou JT, Williams AP (2016) Impact of anthropogenic climate change on wildfire across western US forests. *Proceedings of the National Academy of Sciences* **113**, 11770–11775. doi:10.1073/pnas.1607171113

Bauer HS, Muppa SK, Wulfmeyer V, Behrendt A, Warrach-Sagi K, Späth F (2020) Multi-nested WRF simulations for studying planetary boundary layer processes on the turbulence-permitting scale in a realistic mesoscale environment. *Tellus, Series A: Dynamic Meteorology and Oceanography* **72**, 1761740. doi:10.1080/16000870.2020.1761740

Benjamin SG, Weygandt SS, Brown JM, Hu M, Alexander CR, Smirnova TG, Olson JB, James EP, Dowell DC, Grell GA, Lin H, Peckham SE, Smith TL, Moninger WR, Kenyon JS, Manikin GS (2016) A North American Hourly Assimilation and Model Forecast Cycle: The Rapid Refresh. *Monthly Weather Review* **144**, 1669–1694. doi:10.1175/MWR-D-15-0242.1

Brewer MJ, Clements CB (2020) The 2018 Camp Fire: Meteorological Analysis Using In Situ Observations and Numerical Simulations. *Atmosphere* **11**, 47. doi:10.3390/ATMOS11010047

Chen F, Dudhia J (2001) Coupling an advanced land surface–hydrology model with the Penn State–NCAR MM5 modeling system. Part I: Model implementation and sensitivity. *Monthly Weather Review* **129**, 569–585. doi:10.1175/1520-0493(2001)129<0569:CAALSH>2.0.CO;2

Clements CB, Kochanski AK, Seto D, Davis B, Camacho C, Lareau NP, Contezac J, Restaino J, Heilman WE, Krueger SK, Butler B, Ottmar RD, Vihnanek R, Flynn J, Filippi J-B, Barboni T, Hall DE, Mandel J, Jenkins MA, O'Brien J, Hornsby B, Teske C (2019) The FireFlux II experiment: a model-guided field experiment to improve understanding of fire–atmosphere interactions and fire spread. *International Journal of Wildland Fire* **28**, 308–326. doi:10.1071/WF18089

Coen JL, Cameron M, Michalakes J, Patton EG, Riggan PJ, Yedinak KM (2013) WRF-Fire: Coupled Weather–Wildland Fire Modeling with the Weather Research and Forecasting Model. *Journal of Applied Meteorology and Climatology* **52**, 16–38. doi:10.1175/JAMC-D-12-023.1

Deardorff JW (1972) Numerical Investigation of Neutral and Unstable Planetary Boundary Layers. *Journal of the Atmospheric Sciences* **29**, 91–115. doi:10.1175/1520-0469(1972)029<0091:nionau>2.0.co;2

Deardorff JW (1980) Stratocumulus-capped mixed layers derived from a three-dimensional model. *Boundary-Layer Meteorology* **18**, 495–527. doi:10.1007/BF00119502

Dudhia J (1989) Numerical study of convection observed during the Winter Monsoon Experiment using a mesoscale two-dimensional model. *Journal of the Atmospheric Sciences* **46**, 3077–3107. doi:10.1175/1520-0469(1989)046<3077:NSOCOD>2.0.CO;2

Finney MA (1998) FARSITE: Fire Area Simulator-model development and evaluation. Research Paper RMRS-RP-4, Revised 2004. 47 p. (Ogden, UT: US Department of Agriculture, Forest Service, Rocky Mountain Research Station) doi:10.2737/RMRS-RP-4

Forthofer JM, Butler BW, Wagenbrenner NS (2014) A comparison of three approaches for simulating fine-scale surface winds in support of wildland fire management. Part I. Model formulation and comparison against measurements. *International Journal of Wildland Fire* **23**, 969–981. doi:10.1071/WF12089

Giannaros TM, Lagouvardos K, Kotroni V (2020) Performance Evaluation of an Operational Rapid Response Fire Spread Forecasting System in the Southeast Mediterranean (Greece). *Atmosphere* **11**, 1264. doi:10.3390/atmos11111264

Haupt SE, Kosovic B, Shaw W, Berg LK, Churchfield M, Cline J, Draxl C, Ennis B, Koo E, Kotamarthi R, Mazzaro L, Mirocha J, Moriarty P, Muñoz-Esparza D, Quon E, Rai RK, Robinson M, Sever G (2019) On bridging a modeling scale gap: Mesoscale to microscale coupling for wind energy. *Bulletin of the American Meteorological Society* **100**, 2533–2550. doi:10.1175/BAMS-D-18-0033.1

Hersbach H, Bell B, Berrisford P, Hirahara S, Horányi A, Muñoz-Sabater J, Nicolas J, Peubey C, Radu R, Schepers D, Simmons A, Soci C, Abdalla S, Abellan X, Balsamo G, Bechtold P, Biavati G, Bidlot J, Bonavita M, Chiara GD, Dahlgren P, Dee D, Diamantakis M, Dragani R, Flemming J, Forbes R, Fuentes M, Geer A, Haimberger L, Healy S, Hogan RJ, Hólm E, Janisková M, Keeley S, Laloyaux P, Lopez P, Lupu C, Radnoti G, Rosnay Pd, Rozum I, Vamborg F, Villaume S, Thépaut J-N (2020) The ERA5 global reanalysis. *Quarterly Journal of the Royal Meteorological Society* **146**, 1999–2049. doi:10.1002/QJ.3803

Homer C, Dewitz J, Yang L, Jin S, Danielson P, Xian G, Coulston J, Herold N, Wickham J, Megown K (2015) Completion of the 2011 National Land Cover Database for the conterminous United States – representing a decade of land cover change information. *Photogrammetric Engineering & Remote Sensing* **81**, 345–354. Available at http://www.ingentaconnect.com/content/asprs/pers/2015/00000081/00000005/art00002.

Hong SY, Dudhia J, Chen SH (2004) A revised approach to ice microphysical processes for the bulk parameterization of clouds and precipitation. *Monthly Weather Review* **132**, 103–120. doi:10.1175/1520-0493(2004)132<0103:ARATIM>2.0.CO;2

Iacono MJ, Delamere JS, Mlawer EJ, Shephard MW, Clough SA, Collins WD (2008) Radiative forcing by long-lived greenhouse gases: Calculations with the AER radiative transfer models. *Journal of Geophysical Research: Atmospheres* **113**, D13103. doi:10.1029/2008JD009944

Jiménez PA, Dudhia J, González-Rouco JF, Navarro J, Montávez JP, García-Bustamante E (2012) A Revised Scheme for the WRF Surface Layer Formulation. *Monthly Weather Review* **140**, 898–918. doi:10.1175/MWR-D-11-00056.1

Jiménez PA, Muñoz-Esparza D, Kosović B (2018*a*) A High Resolution Coupled Fire–Atmosphere Forecasting System to Minimize the Impacts of Wildland Fires: Applications to the Chimney Tops II Wildland Event. *Atmosphere* **9**, 197. doi:10.3390/ATMOS9050197

Jimenez PA, Brown B, Kosovic B, Cowie J, Munoz-Esparza D, Anderson A, Petzke B, Boehnert J, Sampson KM, Mahoney WPI, Knievel JC (2018*b*) Description and evaluation of the Colorado Fire Prediction system (CO-FPS). *AGUFM* **2018**, EP31B-03. Available at https://ui.adsabs.harvard.edu/abs/2018AGUFMEP31B..03J/abstract

Knievel JC, Bryan GH, Hacker JP (2007) Explicit Numerical Diffusion in the WRF Model. *Monthly Weather Review* **135**, 3808–3824. doi:10.1175/2007MWR2100.1

Knievel JC, Kosovic B, Cowie J, Anderson A, Boehnert J, Brown B, Brucker D, Chartier N, DeCastro A, Frediani ME, Hahn D, Haupt SE, Jimenez PA, Juliano TW, Mahoney WPI, Munoz-Esparza D, Petzke B, Sampson KM (2020) A Modeling System for Predicting the Behavior of Wildland Fires by Simulating Their Two-Way Interaction with the Atmosphere. *AGUFM* **2020**, A143–0003. Available at https://ui.adsabs.harvard.edu/abs/2020AGUFMA143.0003K/abstract

Kochanski AK, Jenkins MA, Mandel J, Beezley JD, Clements CB, Krueger S (2012) Evaluation of WRF-Sfire Performance with Field Observations from the FireFlux experiment. *Geoscientific Model Development Discussions* **6**, 121–169. doi:10.5194/gmdd-6-121-2013

Kochanski AK, Jenkins MA, Mandel J, Beezley JD, Krueger SK (2013) Real time simulation of 2007 Santa Ana fires. *Forest Ecology and Management* **294**, 136–149. doi:10.1016/j.foreco.2012.12.014

Ladwig W (2017) wrf-python (Version 1.3.4) [Software]. Boulder, Color. UCAR/NCAR. Available at doi:10.5065/D6W094P1

Lai S, Chen H, He F, Wu W (2020) Sensitivity Experiments of the Local Wildland Fire with WRF-Fire Module. *Asia-Pacific Journal of Atmospheric Sciences* **56**, 533–547. doi:10.1007/s13143-019-00160-7

Lareau NP, Donohoe A, Roberts M, Ebrahimian H (2022) Tracking Wildfires with Weather Radars. *Journal of Geophysical Research: Atmospheres* **127**, e2021JD036158. doi:10.1029/2021JD036158

Lautenberger C (2013) Wildland fire modeling with an Eulerian level set method and automated calibration. *Fire Safety Journal* **62**, 289–298. doi:10.1016/j.firesaf.2013.08.014

Li Y, Tong DQ, Ngan F, Cohen MD, Stein AF, Kondragunta S, Zhang X, Ichoku C, Hyer EJ, Kahn RA (2020) Ensemble $PM_{2.5}$ Forecasting During the 2018 Camp Fire Event Using the HYSPLIT Transport and Dispersion Model. *Journal of Geophysical Research: Atmospheres* **125**, e2020JD032768. doi:10.1029/2020JD032768

Linn RR (1997) 'A transport model for prediction of wildfire behavior'. LA-13334-T. (Los Alamos National Laboratory: Los Alamos, NM) doi:10.2172/505313

Littell JS, Mckenzie D, Peterson DL, Westerling AL (2009) Climate and wildfire area burned in western U.S. ecoprovinces, 1916–2003. *Ecological Applications* **19**, 1003–1021. doi:10.1890/07-1183.1

Mandel J, Beezley JD, Kochanski AK (2011) Coupled atmosphere-wildland fire modeling with WRF 3.3 and SFIRE 2011. *Geoscientific Model Development* **4**, 591–610. doi:10.5194/gmd-4-591-2011

Maranghides A, Link E, Mell W, Hawks S, Wilson M, Brewer W, Brown C, Vihnaneck B, Walton WD (2021) A Case Study of the Camp Fire – Fire Progression Timeline. Technical Note (NIST TN) - 2135 (NIST: Gaithersburg, MD) doi:10.6028/NIST.TN.2135

Mass CF, Ovens D (2021) The Synoptic and Mesoscale Evolution Accompanying the 2018 Camp Fire of Northern California. *Bulletin of the American Meteorological Society* **102**, E168–E192. doi:10.1175/BAMS-D-20-0124.1

Mazzaro LJ, Muñoz-Esparza D, Lundquist JK, Linn RR (2017) Nested mesoscale-to-LES modeling of the atmospheric boundary layer in the presence of under-resolved convective structures. *Journal of Advances in Modeling Earth Systems* **9**, 1795–1810. doi:10.1002/2017MS000912

Mell W, Jenkins MA, Gould J, Cheney P (2007) A physics-based approach to modelling grassland fires. *International Journal of Wildland Fire* **16**, 1–22. doi:10.1071/WF06002

Miller DAB (1991) Huygens's wave propagation principle corrected. *Optics Letters* **16**, 1370. doi:10.1364/OL.16.001370

Muñoz-Esparza D, Kosović B, Mirocha J, van Beeck J (2014) Bridging the Transition from Mesoscale to Microscale Turbulence in Numerical Weather Prediction Models. *Boundary-Layer Meteorology* **153**, 409–440. doi:10.1007/s10546-014-9956-9

Muñoz-Esparza D, Lundquist JK, Sauer JA, Kosović B, Linn RR (2017) Coupled mesoscale-LES modeling of a diurnal cycle during the CWEX-13 field campaign: From weather to boundary-layer eddies. *Journal of Advances in Modeling Earth Systems* **9**, 1572–1594. doi:10.1002/2017MS000960

Muñoz-Esparza D, Kosović B, Jiménez PA, Coen JL (2018) An Accurate Fire-Spread Algorithm in the Weather Research and Forecasting Model Using the Level-Set Method. *Journal of Advances in Modeling Earth Systems* **10**, 908–926. doi:10.1002/2017MS001108

Nakanishi M, Niino H (2006) An Improved Mellor–Yamada Level-3 Model: Its Numerical Stability and Application to a Regional Prediction of Advection Fog. *Boundary-Layer Meteorology* **119**(2), 397–407. doi:10.1007/S10546-005-9030-8

Papadopoulos GD, Pavlidou F-N (2011) A Comparative Review on Wildfire Simulators. *IEEE Systems Journal* **5**, 233–243. doi:10.1109/JSYST.2011.2125230

Rooney B, Wang Y, Jiang JH, Zhao B, Zeng Z-C, Seinfeld JH (2020) Air quality impact of the Northern California Camp Fire of November 2018. *Atmospheric Chemistry and Physics* **20**, 14597–14616. doi:10.5194/ACP-20-14597-2020

Rothermel RC (1972) 'A mathematical model for predicting fire spread in wildland fuels.' (Intermountain Forest & Range Experiment Station, Forest Service, U.S. Dept. of Agriculture) Available at https://books.google.pt/books?id=AfyMv5NBSjoC

Scott JH, Burgan RE (2005) Standard fire behavior fuel models: a comprehensive set for use with Rothermel's surface fire spread model. General Technical Reports RMRS-GTR-153. 72 p. (Fort Collins, CO: US Department of Agriculture, Forest Service, Rocky Mountain Research Station) doi:10.2737/RMRS-GTR-153

Shamsaei K, Juliano TW, Igrashkina N, Ebrahimian H, Kosovic B, Taciroglu E (2022) WRF-Fire Wikipage. doi:10.5281/zenodo.6667633

Skamarock WC, Klemp JB, Dudhi J, Gill DO, Barker DM, Duda MG, Huang X-Y, Wang W, Powers JG (2008) A Description of the Advanced Research WRF Version 4.3. doi:10.5065/D6DZ069T

Sullivan AL (2009) Wildland surface fire spread modelling, 1990–2007. 1: Physical and quasi-physical models. *International Journal of Wildland Fire* **18**, 349–368. doi:10.1071/WF06143

Visualization & Analysis Systems Technologies (2022) 'Visualization and Analysis Platform for Ocean, Atmosphere, and Solar Researchers (VAPOR version 3.6.1) [Software].' (UCAR/NCAR - Comput. Inf. Syst. Lab.: Boulder, CO) doi:10.5065/d6j38qhc

Wang D, Guan D, Zhu S, Kinnon MM, Geng G, Zhang Q, Zheng H, Lei T, Shao S, Gong P, Davis SJ (2021) Economic footprint of California wildfires in 2018. *Nature Sustainability* **4**, 252–260. doi:10.1038/s41893-020-00646-7

Westerling AL (2016) Increasing western US forest wildfire activity: sensitivity to changes in the timing of spring. *Philosophical Transactions of the Royal Society B: Biological Sciences* **371**, 20150178. doi:10.1098/RSTB.2015.0178

Westerling AL, Hidalgo HG, Cayan DR, Swetnam TW (2006) Warming and earlier spring increase Western U.S. forest wildfire activity. *Science* **313**, 940–943. doi:10.1126/science.1128834

WRF (2020) User's Guide for the Advanced Research WRF (ARW) Modeling System Version 4.2. Available at https://www2.mmm.ucar.edu/wrf/users/docs/user_guide_v4/v4.2/contents.html [accessed 11 June 2022]

Wyngaard JC (2004) Toward Numerical Modeling in the "Terra Incognita". *Journal of the Atmospheric Sciences* **61**, 1816–1826. doi:10.1175/1520-0469(2004)061<1816:TNMITT>2.0.CO;2

Xu K-M, Randall DA (1996) A Semiempirical Cloudiness Parameterization for Use in Climate Models. *Journal of the Atmospheric Sciences* **53**, 3084–3102. doi:10.1175/1520-0469(1996)053<3084:ASCPFU>2.0.CO;2

Data availability. All data, models, or codes that support the findings of this study are available from the corresponding author upon reasonable request.

Conflicts of interest. The authors declare no conflicts of interest.

Declaration of funding. This work is supported through the National Science Foundation's Leading Engineering for America's Prosperity, Health, and Infrastructure (LEAP HI) program by grant number CMMI-1953333. The opinions and perspectives expressed in this study are those of the authors and do not necessarily reflect the views of the sponsor.

Acknowledgements. We acknowledge high-performance computing support from Cheyenne (doi:10.5065/D6RX99HX) provided by NCAR's Computational and Information Systems Laboratory, sponsored by the National Science Foundation.

Author affiliations

[A]Department of Civil and Environmental Engineering, University of Nevada-Reno, Reno, NV, USA.

[B]National Center for Atmospheric Research, Boulder, CO, USA.

[C]Department of Physics, University of Nevada-Reno, Reno, NV, USA.

[D]Department of Civil and Environmental Engineering, University of California-Los Angeles (UCLA), Los Angeles, CA, USA.